crystals

MDPI

Review

Next-Generation Quantum Materials for Thermoelectric Energy Conversion

Shiva Kumar Singh *, Julian Munevar, Letícia Mendonça-Ferreira and Marcos A. Avila *

CCNH, Universidade Federal do ABC (UFABC), Santo André 09210-580, SP, Brazil
* Correspondence: shivanpl@gmail.com (S.K.S.); avila@ufabc.edu.br (M.A.A.)

Abstract: This review presents the recent advances in the search for thermoelectric (TE) materials, mostly among intermetallic compounds and in the enhancement of their TE performance. Herein, contemporary approaches towards improving the efficiency of heat–electricity conversion (e.g., energy harvesting and heat pumping) are discussed through the understanding of various emergent physical mechanisms. The strategies for decoupling the individual TE parameters, as well as the simultaneous enhancement of the TE power factor and the suppression of heat conduction, are described for nanoparticle-doped materials, high entropy alloys, and nanowires. The achievement of a superior TE performance due to emergent quantum phenomena is discussed for intermetallic chalcogenides and related systems (e.g., strong and weak topological insulators, Weyl and Dirac semimetals), and some of the most promising compounds within these classes are highlighted. It was concluded that high-entropy alloying provides a methodological breakthrough for employing band engineering methods along with various phonon scattering mechanisms towards significant TE efficiency improvement in conventional TE materials. Finally, topological semimetals and magnetic semimetals with several intriguing features, such as a violation of the Wiedemann–Franz law and outstanding perpendicular Nernst signals, are presented as strong candidates for becoming next-generation TE quantum materials.

Keywords: thermoelectric; quantum materials; high entropy alloys; nanowires; topological insulators; semimetals

Citation: Singh, S.K.; Munevar, J.; Mendonça-Ferreira, L.; Avila, M.A. Next-Generation Quantum Materials for Thermoelectric Energy Conversion. *Crystals* **2023**, *13*, 1139. https://doi.org/10.3390/cryst13071139

Academic Editor: Sergey L. Bud'ko

Received: 30 June 2023
Revised: 15 July 2023
Accepted: 17 July 2023
Published: 21 July 2023

1. Introduction

Materials science and condensed matter physics are the primary driving forces for the discovery and understanding of next-generation green and renewable energy materials demanded by the 21st Century. Thermoelectric (TE) materials offer potentially significant contributions in this matrix by recycling waste heat. Over the past decades, it has become clear that if TE devices are to expand beyond their currently limited *niche* markets, next-generation materials exploring unconventional electronic and/or thermal phenomena need to be designed, discovered, and optimized. In this context, we highlighted the current research focus towards the discovery and development of novel quantum TE materials, as well as the strategies for the performance enhancement of these materials in TE devices.

TE devices can harvest waste heat from the Sun, industrial machines, automobiles, and even from our bodies, converting it into useful electricity. In addition, TE devices have many advantages, such as a good reliability, fast response, and low noise [1–3]. A primary goal of the research and development in TE materials is the enhancement of their efficiency in heat $\longleftrightarrow$ electricity conversion, which is quantified by the material's figure of merit $ZT = S^2\sigma T/(\kappa_e + \kappa_L)$. This is a dimensionless parameter where S, σ, κ_e, and κ_L are the thermopower, electrical conductivity, electronic thermal conductivity, and lattice thermal conductivity, respectively (all of which are temperature-dependent quantities). TE materials are basically those capable of transforming heat into useful electric energy

by using the Seebeck effect or reversing the heat flow by applying a voltage using the Peltier effect.

The direct conversion of thermal to electrical energy (the Seebeck effect) can be understood with the help of a schematic (Figure 1) based on the equation for conductivity (Equation (1), discussed in the next section). The charge flows due to the temperature differences between the higher temperature ("hot") and lower temperature ("cold") sides of n-type (electrons as majority carrier) and p-type (holes as majority carriers) semiconducting materials are shown in the (a) and (b) panels, respectively. The schematic of the energy bands and the plot for the density of states Fermi function f(ε) with carrier energy (ε) are overlapped for convenience and are not on the same scale. Near the Fermi level (ε_F) in the *n*-type semiconductors, the hot side will have a higher number of occupied energy states (compared to the cold side) and/or states with higher energy above the bottom of the conduction band (ε_C). Thus, more electrons will flow from the hot to the cold side in the *n*-type semiconductors. Conversely, near ε_F in the *p*-type semiconductors, the cold side has a higher number of occupied energy states and/or states with higher energy below the top of the valence band (ε_V), so more electrons will flow from the cold to the hot side (equivalent to the holes flowing from the hot to the cold side).

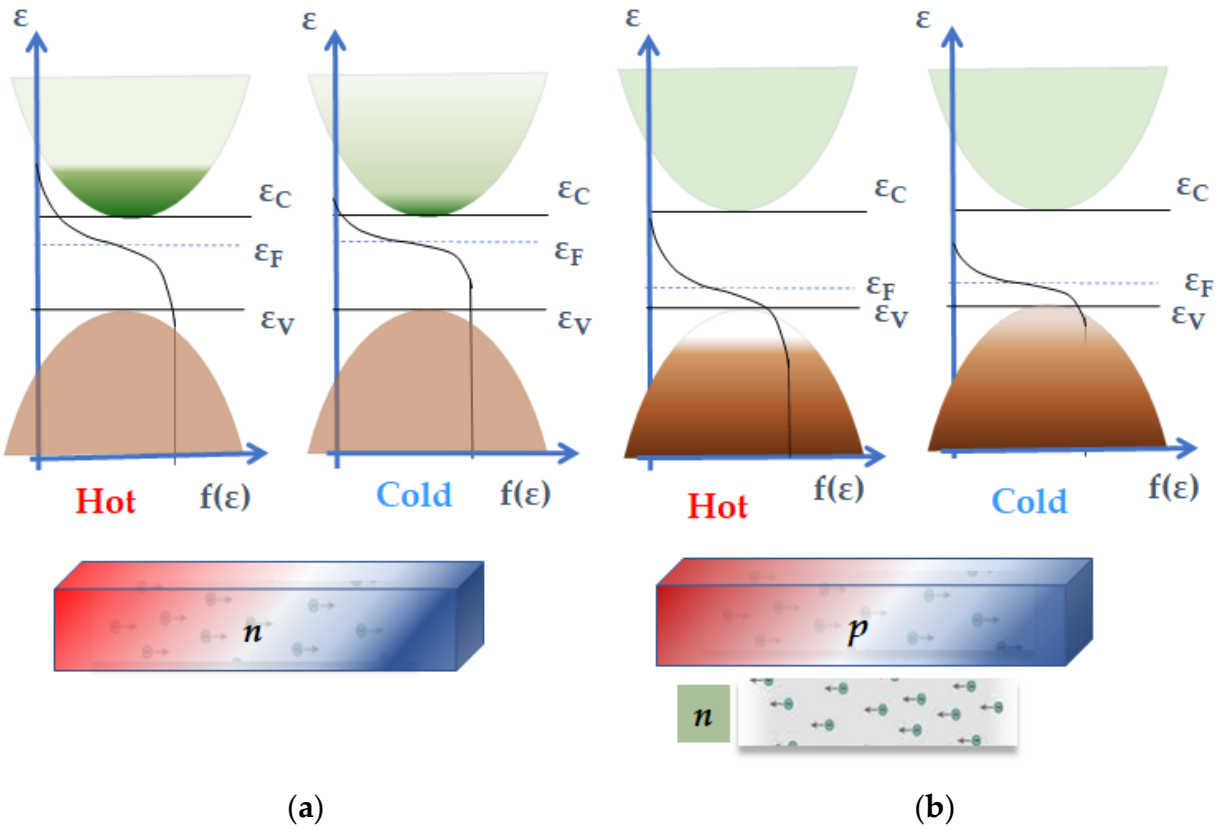

Figure 1. Schematic of the charge flow due to the temperature difference between the higher temperature ("hot") and lower temperature ("cold") sides of (**a**) an *n-type* semiconductor with electrons as the majority carrier and (**b**) a *p-type* semiconductor with holes as the majority carriers. The energy band diagram and the distribution of the density of states (DOS) are overlapped for visual representation.

Similarly, if we apply a potential difference across a material, there will be a shift in ε_F along its sides and electrons will flow from the higher ε_F side to the lower ε_F side. These moving charges will transfer heat with an energy level equal to the difference between the highest occupied level and the Fermi level ε_F. This phenomenon is known as the Peltier effect. Essentially, these two separately identified physical phenomena lead to electrical energy generation and reverse the flow of heat (TE cooling), respectively.

An ideal TE material should have a large S, which is usually the case of semiconductors, a high σ as found in good metals, and a low κ as found in glasses. In its most concise representation, an ideal TE material may be identified as a "phonon-glass, electron-crystal" (PGEC), as proposed by Slack [4]. The ZT parameter should be as large as possible because it is directly related to the material's thermodynamic conversion efficiency at the operating temperature range T_H–T_C [5,6], whose maximum value (η_{max}) in a TE device is given by Equation (1).

$$\eta_{max} = \eta_C \frac{\sqrt{1 + ZT_{avg}} - 1}{\sqrt{1 + ZT_{avg}} + \frac{T_C}{T_H}} \quad (1)$$

where η_C is the Carnot efficiency; T_C and T_H are the cold- and hot-side temperatures, respectively; $T_{avg} = (T_C + T_H)/2$; and ZT_{avg} is the dimensionless TE figure of merit of the material at T_{avg}. Competitive TE applications not only require a high peak ZT but also require a high ZT_{avg} in a wide temperature range [1,2]. Thus, further improvement of the peak ZT/ZT_{avg} is inevitable. The main hurdle in improving the device performance is that the three physical quantities S, σ, and κ_e are interdependent solid-state quantities derived from the same electronic free energy. Therefore, the optimization of one often degrades another (or both others). For example, improving the electronic conductivity with dopants leads to a simultaneous increase in the electronic contribution of the thermal conductivity via the Wiedemann–Franz (WF) law $\kappa = \sigma LT$ (where L is the Lorenz number). Nevertheless, several applications (Figure 2) using the current level of efficiency were conceived and implemented to a certain extent [7].

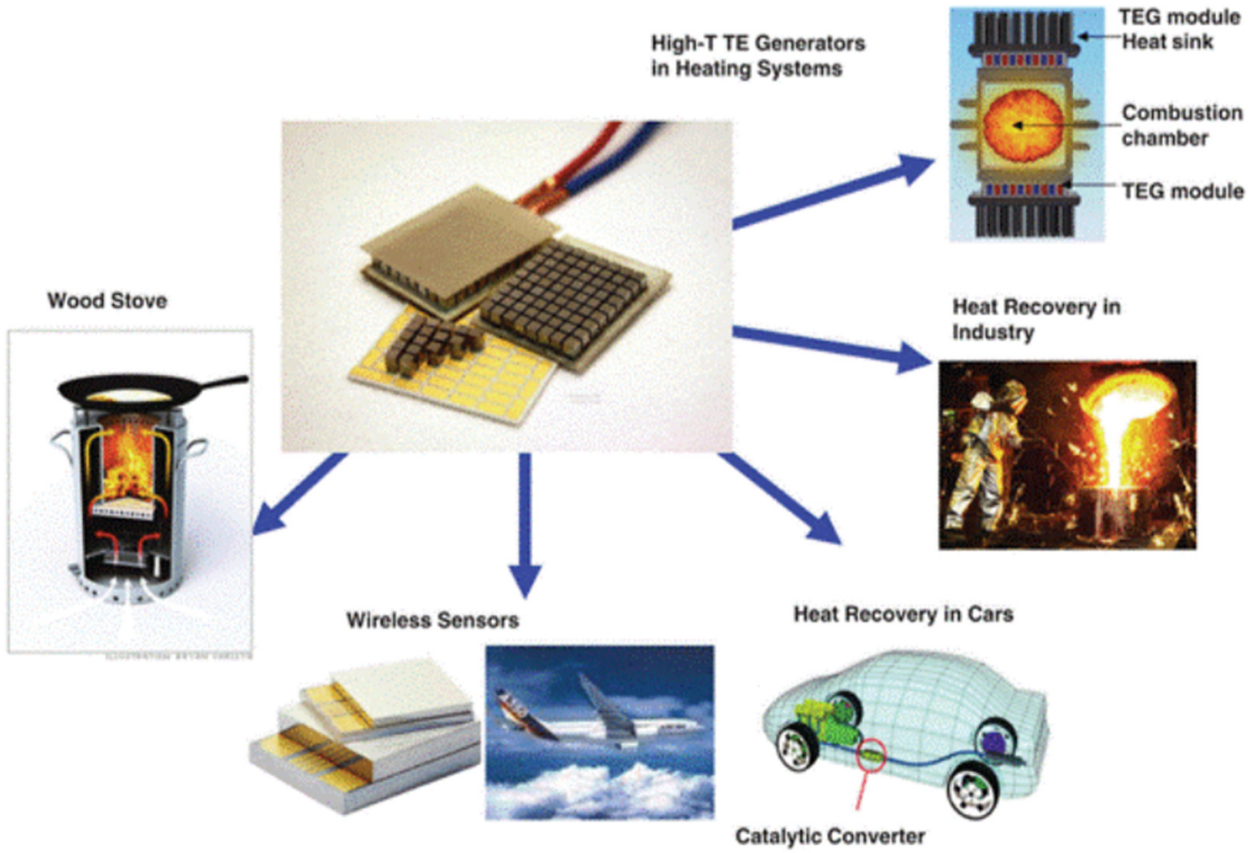

Figure 2. Various applications of thermoelectric materials as energy generators/converters [reprinted with permission of Ref. [7] and Wiley materials, Copyright (2016) John Wiley and Sons].

The ZT values for the bulk materials currently in commercial use are in the range of 0.8–1.1 [3] and represent an energy conversion efficiency of approx. 10% in the final device. The widespread use of TE devices in various areas would require a ZT of at least two [1,8].

From the commercial perspective, in comparison to the price of solar and wind power (less than US$1/watt), the minimum cost of TE devices at approx. US$50/watt for mid-temperature range (500–800 K) power generation [9–11] is not yet competitive. For most applications, it represents another crucial factor that needs to be considered in addition to its overall efficiency [12]. Therefore, the ZT should be maximized [11], ideally aiming for at least ZT = 4 if TE devices are to become competitive with fossil fuel engines [8].

The recent TE research demonstrates outstanding progress, with quite encouraging advances [13–18]. Using a *big data* survey, a golden Seebeck coefficient range of 200–230 μV/K for TE semiconductors with lattice thermal conductivities of 0.4–1.5 W/m-K [19] was established. Peak ZT values close to 2.5 were achieved for some TE materials, due to a simultaneous enhancement of the power factor (PF) $S^2\sigma$ and a significant reduction in the κ_L. Theoretically, the latter cannot be reduced below a minimum (amorphous limit) [20], implying a threshold for ZT improvement using nano-structuring and other means for κ_L suppression. In contrast, the manipulation of the PF for improvement has no theoretical limit, offering a wide vista for achieving a higher ZT [21]. We can divide the strategies for ZT enhancement into three subgroups: (i) an increase in the PF ($S^2\sigma$); (ii) a reduction in the κ_L; and (iii) a simultaneous enhancement in the PF and reduction in the κ_L. These strategies rely on decoupling the electronic and phonon sub-systems through various methods and are explained in the following sections by exploring the individual TE parameters.

2. Strategies to Improve the TE Parameters

2.1. Enhancement of the PF ($S^2\sigma$)

The transport coefficients are given by the solutions of the Boltzmann equations (Equations (2)–(4)) [22].

$$\sigma = e^2 \int d\varepsilon \left(-\frac{\partial f}{\partial \varepsilon}\right) \Sigma(\varepsilon) \tag{2}$$

$$S = \frac{e}{T\sigma} \int d\varepsilon \left(-\frac{\partial f}{\partial \varepsilon}\right) \Sigma(\varepsilon)(\varepsilon - \varepsilon_F) \tag{3}$$

$$K_e = \left[\frac{1}{Te^2} \int d\varepsilon \left(-\frac{\partial f}{\partial \varepsilon}\right) \Sigma(\varepsilon)(\varepsilon - \varepsilon_F)^2\right] \tag{4}$$

where e is the electron charge, $\left(-\frac{\partial f}{\partial \varepsilon}\right)$ is the Taylor expansion for the change in the density of states near ε_F in the energy range of ε and $\varepsilon + d\varepsilon$, and $\Sigma(\varepsilon)$ is the transport distribution function (TDF) [22] given by the following.

$$\Sigma(\varepsilon) = \sum \delta(\varepsilon - \varepsilon(k))\tau(k)v_k(k)^2 \tag{5}$$

Here, the summation is over the first Brillouin zone, where $v_k(k)$ is the group velocity of the carriers with wave vector k in the direction of the applied field, $\tau(k)$ is the carrier lifetime, and $\varepsilon(k)$ is the dispersion relation for the carriers. If many bands contribute to the transport process, the summation is extended to all the bands [22]. Let us consider the case of parabolic bands, in which the transport distribution is simplified to the following.

$$\Sigma(\varepsilon) = g(\varepsilon)\tau(\varepsilon, T)v_x(\varepsilon)^2 \tag{6}$$

where $g(\varepsilon)$ is the density of states (DOS). In bulk (3D) semiconductors, $g(\varepsilon)$ with a spin degeneracy factor of two is generally given by the following.

$$g_{3D}(\varepsilon) = 8\pi \left(\frac{m^*}{h^2}\right)^{3/2} (\varepsilon - \varepsilon_C)^{1/2} \tag{7}$$

where m^* is the DOS effective mass of the charge carrier and h is the Planck constant. Using these equations, we can understand the relevance of the basic TE factors, such as

the m^*, carrier concentration (n), carrier mobility (μ), and their influence on the PF. For example, σ is higher in metals due to a higher carrier concentration. However, it is also responsible for a higher κ_e and, since $(\varepsilon - \varepsilon_F)$ will be very small for metals, leads to a poor S (Equation (3)). The optimum performance (peak PF value) is obtained for heavily doped bulk semiconductors with n to the order 10^{19}–10^{21} cm^{-3} [23].

With respect to the carrier scattering mechanisms, it is clear from Equation (5) that the carrier relaxation time (τ) and its energy dependence $\tau(\varepsilon)$ are other parameters through which σ and S can be manipulated. The carrier mobility μ represents the relaxation time τ, which is related to its average $\overline{\tau}$, as shown in Equation (8).

$$\mu = \frac{e\overline{\tau}}{m^*} \tag{8}$$

Therefore, μ has a direct impact on σ through τ (Equations (2) and (5)), and $\tau(\varepsilon)$ can be approximately expressed in the following form.

$$\tau(\varepsilon) = \tau_0 \varepsilon^r, \tag{9}$$

where τ_0 and r are the constants for the given scattering mechanism. The dependence of the PF on the scattering parameter r can be understood through the following relation [24,25].

$$S^2\sigma \propto \frac{\varepsilon^r}{m^*}\frac{{k_B}^2}{e}\left\{\frac{\varepsilon_F - \varepsilon_c}{k_B T} + \left(r + \frac{5}{2}\right)\right\}^2, \tag{10}$$

which implies that larger r values lead to higher peak PFs. In semiconductors, $r = -1/2$, $1/2$, and $3/2$ for the acoustic phonon scattering, optical phonon scattering, and impurity scattering, respectively. The high scattering rates of the carriers can be achieved by introducing ionized/magnetic impurities as additional scattering centers [26–29].

On the other hand, it is inferred from Equation (10) that a lower effective mass m^* is beneficial for the PF, albeit through a complicated effect. A large m^* and a low n cause an increase in μ and σ but a decrease in S (and vice versa). Rigorously, however, the m^* in S and the m^* in σ are not the same [30,31], so the former is termed the *Seebeck effective mass* ($m_s{}^*$) and the latter expressed as $m_c{}^*$. These two effective masses are related through the effective valley degeneracy (N_V) and the effective carrier pocket anisotropy (K) [$m_s{}^* = (N_v K)^{2/3} m_c{}^*$]. The relation between both effective masses is discussed extensively in Refs. [30,31]. The strategies that manipulate S show that a higher $m_s{}^*$ is beneficial, whereas the routes that manipulate σ show that a lower $m_c{}^*$ is beneficial. However, the manipulation of one (σ or S) must not affect the other adversely. Similarly, a higher S value can be achieved through rapid changes in the TDF (Equation (5)) around ε_F due to the manipulation of either $g(\varepsilon)$ or τ. One strategy for using these structures is to design materials with $g(\varepsilon)$ that deviates from the $\varepsilon^{1/2}$ dependence. Particularly, a δ-function-like TDF can be approximated if there is a drastic change in $g(\varepsilon)$ around ε_F. A notable example is the concept of *resonant state doping*, in which a resonance in the DOS is achieved using chemical doping [18,32–34].

Most of the band structure engineering strategies, such as the quantum confinement of carriers, valley degeneracy, and band resonance, are based on manipulating these parameters and balancing them for an optimum PF. Similarly, carrier modification schemes such as carrier energy filtering, carrier pocket engineering, and modulation layer doping, manipulate the PF by altering σ and S. These schemes have been compiled in seminal reviews [23,25,34–36]. Apart from σ and S, thermal conductivity κ is another parameter whose minimization leads to an enhanced ZT, which we will discuss in next section.

2.2. Reduction in the κ_L

Thermal conductivity is the sum of the electronic and lattice contributions ($\kappa = \kappa_e + \kappa_L$). κ_e cannot be limited without the undesirable effect of limiting σ (unless practical violations of the WF law can be found). However, by minimizing κ_L, the ZT has been found to improve significantly. In fact, κ_L is the only independent parameter of the TE figure of

merit. In crystalline solids, thermal energy combined with the interactions between atoms produces vibrations around their equilibrium positions, leading to quantized vibrational waves with various frequencies. The quanta of these waves, termed phonons, propagate heat through the lattice. The *phonon dispersion relation*, connecting the phonon wave vector (k_{ph}) with its angular frequency (ω_{ph}) fundamentally determines the phonon transport and the resultant lattice thermal conductivity (κ_L). In the simple case of a 1D single-atom harmonic chain with an atomic mass M, the phonon dispersion relation is given by the following [37].

$$\omega_{ph} = 2\left(\sqrt{\frac{F}{M}}\right)\sin\left(\frac{\pi}{2}\frac{k_{ph}}{k_c}\right) \tag{11}$$

where F and k_c are the force constant and cut-off phonon wave vector, respectively. Fundamentally, the phonon transport can be manipulated through changes in either the M or F, and materials with a large M but a small F tend to show a low κ_L. Various mechanisms have been developed to reduce κ_L by changing the phonon dispersion through such manipulation, and can be broadly categorized into intrinsic and extrinsic approaches. *Rattling* modes in clathrates [26,38], soft localized vibrations [39], strong lattice anharmonicity [40], liquid-like ions [41], and low sound velocity [42] are promising intrinsic mechanisms. Point defects [18,43,44], dislocations [45–47], nano-inclusions/nano-precipitates [17,48], strain [49], and interfaces [48,50] are promising extrinsic mechanisms for achieving an ultra-low (glass-like) κ_L. Both approaches usually focus on the minimization of the phonon relaxation time τ_{ph}. In a conventional crystalline solid, the dependence of the κ_L on τ_{ph} is given as following.

$$\kappa_L = \frac{1}{3}Cv_s l_{ph} = \frac{1}{3}Cv_s^2\tau_{ph} \tag{12}$$

where C is the specific heat capacity, v_s is the sound velocity, and l_{ph} is the phonon mean free path. These parameters and τ_{ph}, specifically, are phonon frequency dependent [51]. Therefore, by exploring the various mechanisms for phonon scattering, κ_L can be minimized. The phonon scattering rates (${\tau_{ph}}^{-1}$) as a function of the phonon frequencies corresponding to various scattering mechanisms are shown in Figure 3 [35]. For example, atomic point defects (formed by elemental substitution, removal, or insertion) introduce modifications in F through lattice strains and/or a change in M, which are effective for scattering short-wavelength phonons.

Nano-sized precipitates/inclusions can significantly scatter medium-wavelength phonons. Mesoscaled grains can scatter phonons of all wavelengths but are more effective for long-wavelength phonons [35,48,52]. The schemes for the κ_L reduction are detailed in other publications [35,36,53].

Many recent reports [40–42,54,55] have used the above-mentioned intrinsic and extrinsic approaches for low κ_L by changing M or F. We will summarize the advances that involve new strategies, and which are also applicable to other materials. For example, when M is constant, anharmonic lattice vibrations correspond to an anharmonicity in F at non-equilibrium atomic positions, which work as a *dynamic* strain [49]. This leads to fluctuations (broadening) in ω_{ph} at a given k_{ph}, which accelerates the change rate of the phonon distribution function and, therefore, enables a shorter relaxation time for the phonons [54]. Using static lattice strains, a remarkable κ_L reduction was achieved in $Na_{0.03}Eu_{0.03}Sn_{0.02}Pb_{0.92}Te$. A high ZT was realized, which was largely derived from the κ_L reduction [49]. A broadening phonon dispersion was found in crystalline solids with weakly bonded heavy constituent elements, leading to a shorter relaxation time for the phonons and a low κ_L [42]. Similarly, both liquid-like ions (weak chemical bonds) and a low-sound velocity [$v_s \propto \sqrt{\frac{F}{M}}$] indicate a small force constant [41,42].

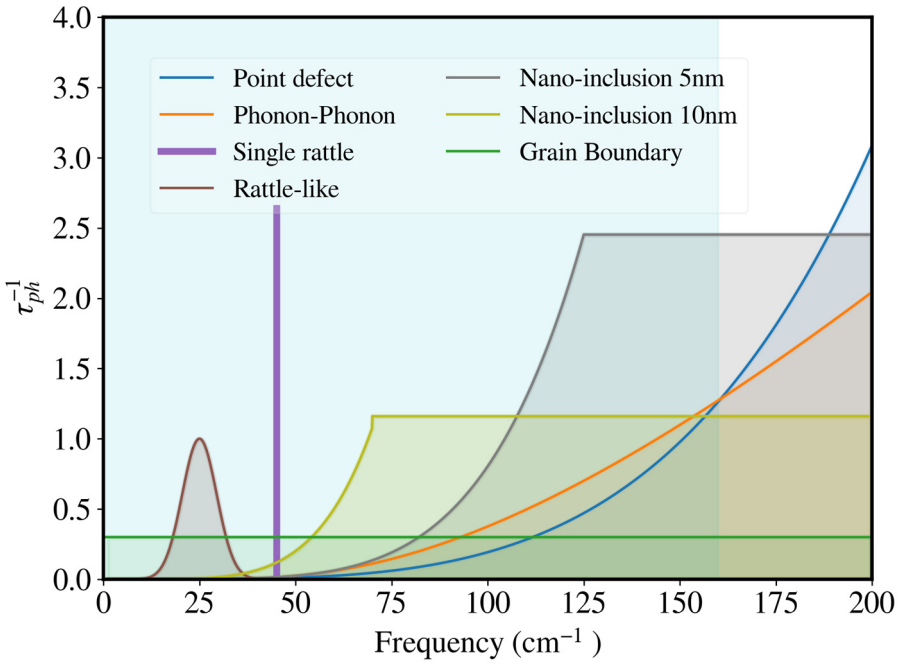

Figure 3. Schematic of the frequency dependence of the phonon scattering rates (τ_{ph}^{-1}) for various scattering mechanisms. Higher scattering rates lead to a lower lattice thermal conductivity κ_L [reproduced from Ref. [35] with permission under a Creative Commons Attribution license, Copyright (2016), Springer Nature and J. Yang et al.].

2.3. Simultaneous Enhancement of the PF and Reduction in the κ_L

We now discuss some powerful strategies which work for various TE materials, although not for all. A first example is the formation of composites with superparamagnetic nanoparticles in the filled skutterudite $CoSb_3$ 26] and in Bi_2Te_3 [56,57]. Such nanoparticles allow for the manipulation of electron and phonon transport at nanometer and mesoscopic length scales [26,58]. The superparamagnetic behavior (magnetized nanoparticles similar to a paramagnet under an external magnetic field) lead to three kinds of thermo-electro-magnetic effects [26]. (*i*) A charge transfer from the magnetic inclusions to the matrix phase (material) leading to interface band bending (Figure 4a) due to their different electronic structures. This results in the emergence of a carrier energy filtering effect at the interfaces between the matrix and the nanoparticle (Figure 4b); (*ii*) In comparison with electron scattering in a ferromagnetic state (Figure 4c), a multiple scattering of electrons occurs similar to the Kondo effect due to superparamagnetic fluctuations (Figure 4d), leading to an increased magnitude of the scattering parameter *r*. (*iii*) Enhanced phonon scattering as a result of both the magnetic fluctuations and the nanostructures. The enhancement in *r* is derived from two aspects: carrier energy filtering and carrier multiple scattering. However, if the work function of the matrix is smaller than the nanoparticles, the carrier filtering doesn't occur, as evidenced in the case of Bi_2Te_3 [56].

Another example of the combination of suppressed κ_L, high σ, and large *S* was achieved in the filled skutterudite $CoSb_3$ [59] through coexisting, multi-localization transport. The enhancement of *r* induced by carrier multiple scattering resulted in a large *S* value, while a significant decrease in κ_L was derived from phonon-localized resonant scattering induced by in-filler rattling. The charge transfer from the filler provided a high σ due to accelerated electron movement.

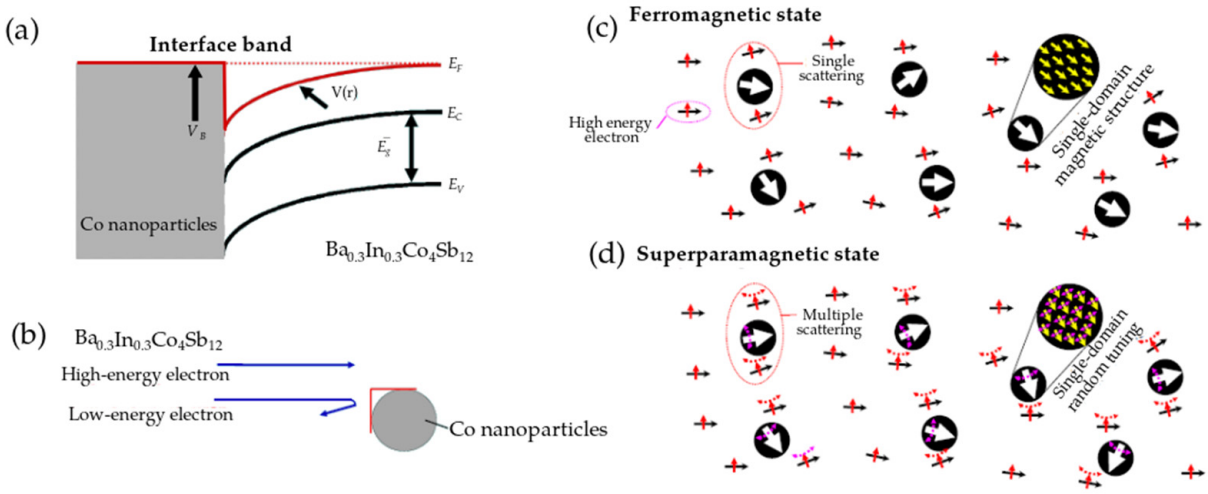

Figure 4. (**a**) Interface band bending due to the charge transfer from the magnetic inclusions to the matrix phase. (**b**) Low electron energy filtering due to band bending at the xCo/$Ba_{0.3}In_{0.3}Co_4Sb_{12}$ interfaces. (**c**) Single scattering due to the ferromagnetic state. (**d**) Multiple scattering of electrons due to the superparamagnetic state of the co-nanoparticles [reprinted with permission of Ref. [26] and Springer Nature, Copyright (2017) Springer Nature].

The superparamagnetic Ni nanoparticles (Ni-NPs) were incorporated into the $Bi_2Te_{2.7}Se_{0.3}$ matrix using a low-temperature and high-pressure sintering method. A 32% increase in the ZT compared to the $Bi_2Te_{2.7}Se_{0.3}$ matrix was observed, reaching 1.1 at 360 K for the Ni/$Bi_2Te_{2.7}Se_{0.3}$ nanocomposites. An improvement in TE performance of the nanocomposite was attributed to an increase in σ due to the charge transfer from the Ni-NPs to the matrix, the enhancement in S from electron multiple scattering, and the reduction in κ_L caused by phonon scattering at the heterointerface [57].

Similarly, discordant [15] and variable [60] ion doping in PbSe was found to improve the TE performance through the simultaneous improvement of the PF and κ_L. The peculiar behavior of the Cu ions in the PbSe-Cu system provided extra charge carriers as the temperature increased, which guaranteed an optimized carrier concentration over a wide temperature range. The vibration of the Cu atoms around the interstitial sites of PbSe led to a reduction in κ_L at high temperatures [60]. For Hg-alloyed PbSe, experiments have shown a significant increase in the Seebeck coefficient due to band convergence. It was observed that the Hg^{2+} cations sat at an off-centered (discordant) position within the PbSe lattice. The DFT calculations indicated that off-centering played an active role in lowering the thermal conductivity, resulting in a ZT of 1.7 at 970 K [15].

Although these powerful strategies work for certain compounds, they cannot be generalized. However, high-entropy alloying and size reduction (nanowires) constitute promising strategies for the simultaneous enhancement of the PF and κ_L reduction, which, at least in principle, may work for all TE materials. We will, thus, discuss these two approaches in the next section as well as the topological systems that have shown great potential as next-generation quantum TE materials.

3. Potential Quantum Materials

3.1. High-Entropy Alloying of Thermoelectric Materials

The concept of high-entropy alloys (HEAs) [61–68] has opened a new platform for designing next-generation materials and could significantly improve the performance of existing materials. HEAs typically refer to solid solutions in which more than five principal elements, each in an equal molar ratio, compete for the same crystallographic site [61–63]. This approach is also known as multi-(principal elements) alloying or equimolar alloying. The high entropy of mixing created due to the presence of several elements overcomes the enthalpy of mixing at the melting temperature, possibly leading to solid solution formation

and eliminating phase segregation [63,68]. For the alloy system, the Gibbs free energy of mixing can be expressed as follows.

$$\Delta G_{mix} = \Delta H_{mix} - T\Delta S_{mix} \quad (13)$$

where ΔG_{mix} is the Gibbs free energy of mixing, ΔH_{mix} is the enthalpy of mixing, ΔS_{mix} is the entropy of mixing, and T is the absolute temperature. It is clear from Equation (13) that, if ΔH_{mix} is kept constant, a higher entropy of mixing will lead to a lower Gibbs free energy and result in a more stable alloy system. The schematic of a solid solution is shown in Figure 5. However, this is not always true. Defining T_m as the average melting point of the alloy system, if the ratio $T_m\Delta S_{mix}/\Delta H_{mix}$ is larger than the unity, the effect of the mixing entropy is greater than that of the enthalpy of mixing at the melting temperature, so the high-entropy phase tends to form. Theoretically, as long as the ratio is greater than the unity, even three elements might form HEAs. The more elements in an equimolar HEA, the higher the entropy of mixing. However, the amount of each element should be higher than 5 at% [61].

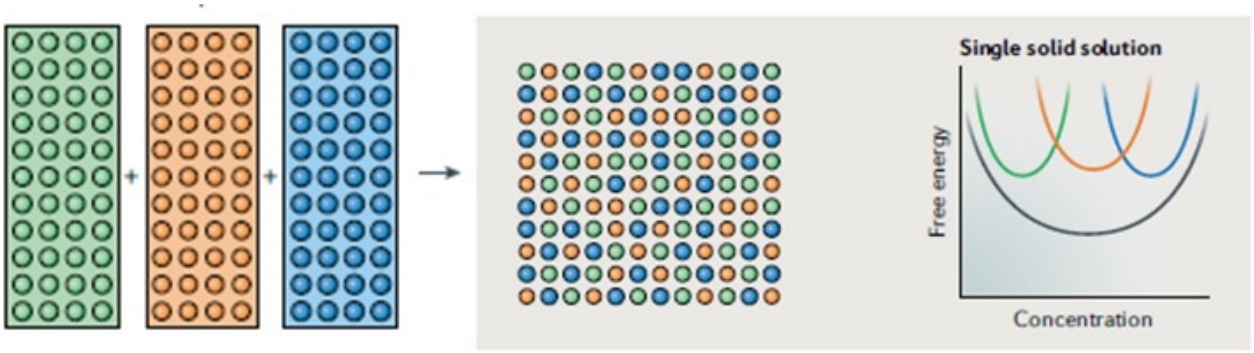

Figure 5. Formation of a single-solid solution when three alloying elements (represented by the green, orange, and blue spheres) are mixed in equal proportions. Some of the other possible reactions that can also occur (not shown in the figure) include spinodal decomposition and multiple solid solutions [reprinted with permission from Ref. [68] and Springer Nature, Copyright (2019) Springer Nature].

For a random alloy system with m components, the configurational entropy of intermixing is given by the following.

$$\Delta S_{mix} = -R\sum_{1}^{m} c_i \ln c_i \quad (14)$$

where R is the gas constant, c_i is the molar content of the i^{th} component , and ΔS_{mix} is the maximum when the components are equimolar. For a Z component, the equimolar system entropy ΔS_{mix} is given by the following [63].

$$\Delta S_{mix} = -R\left[\left(\frac{1}{Z}\right)\ln\left(\frac{1}{Z}\right) + \left(\frac{1}{Z}\right)\ln\left(\frac{1}{Z}\right) + \left(\frac{1}{Z}\right)\ln\left(\frac{1}{Z}\right) + \cdots\cdots + \left(\frac{1}{Z}\right)\ln\left(\frac{1}{Z}\right)\right] = -R\ln\left(\frac{1}{Z}\right) = R\ln Z \quad (15)$$

High-entropy effects increase the number of elements and their solubility limit, providing leverage for designing new materials with emergent properties. Entropy has been identified as a gene-like performance indicator for TEs [69] and works as an effective guide to greatly improve the TE performance, using either a significantly suppressed κ_L to its theoretical minimum value and/or enhancing the crystal structure symmetry to yield large Seebeck coefficients. Four core effects associated with HEAs [61,62] are also pertinent to enhance the TE performance of materials and are described as follows.

(a) ***High-Entropy Effects*:** High entropy of mixing tends to form body-centered cubic (*bcc*), face-centered cubic (*fcc*), or hexagonal (*hcp*) structures. Simple cubic structures are more likely to feature high band degeneracy and, hence, a high PF [61–64]. A higher symmetry leads to larger Seebeck coefficients due to an increase in the DOS

close to the Fermi level. Generally, the compounds with a high crystal symmetry and the valley extrema located at non-Γ low-symmetry points in the Brillouin zone possess a high valley degeneracy N_v [23,70], as in the cases of Bi_2Te_3, SnTe, PbTe, and Mg_2Si [23,70–74]. The increase in N_v was already reported by the band structure calculations, via changing the symmetry of the tetragonal chalcopyrite system from a non-cubic to a pseudo-cubic structure [72]. Through entropy alloying, the rhombohedral structure of $PbGeSnTe_3$ changed to a cubic structure of $PbGeSnCd_xTe_{3+x}$ [75]. Similarly, the monoclinic structure of Cu_2Se changed to hexagonal in the cases of $Cu_2S_{0.5}Te_{0.5}$, $Cu_2S_{0.5}Se_{0.5}$, and $Cu_2Se_{1/3}Te_{1/3}S_{1/3}$ [69]. With an increasing crystal lattice symmetry, the S values increased significantly (Figure 6). On the other hand, the high entropy of mixing also tended to extend the solubility limits of the alloying elements. This provided leverage to manipulate the band structure through the formation of resonant levels. The synergistic band engineering of the resonant levels and band convergence could also be achieved, which was beneficial for larger ZT_{avg}.

(b) ***Sluggish Diffusion Effects*:** The presence of several elements caused some phases to have low diffusion kinetics, which facilitated the in-situ formation of nano-precipitates and nano-inclusions. As discussed earlier, nanostructures can lead to a reduction in κ_L. Acharya et al. recently reported that distorted nanostructures enhanced the TE performance of HEA chalcopyrite [76].

(c) ***Severe Lattice Distortion Effects*:** With several elements in the unit cell, more point defects are created and, due to extensive ionic mass and size mismatches, κ_L can be minimized. This was realized using entropy alloying in $(Cu/Ag)(In/Ga)Te_2$ [69], in the pseudo-ternary compound $(SnTe)_{1-2x}(SnSe)_x(SnS)_x$ [77], and in ZrCoSb-based half-Heusler alloys [78].

(d) ***The Cocktail Effect*:** The presence of multi-constituent elements can lead to the improvement of certain properties. For example, the mechanical strength was significantly improved in $Cu_{2-y}Ag_yTe_{1-2x}S_xSe_x$ [79]. Novel phenomena may also emerge, which is why recent condensed matter research focused on HEAs in various other areas, such as superconductivity, hydrogen storage, magnetism, and shape memory alloys, among others [66].

It is evident from Equation (13) that the stability of a phase is determined by the contributions from both the enthalpy and the entropy of mixing. The equimolar composition possesses the highest entropy, but not necessarily the lowest enthalpy. Therefore, it is not necessarily a solid solution phase [64]. Thus, increasing the number of elements may also lead to the formation of other undesired phases [63,64]. To minimize the enthalpy (the internal strain energy), other factors based on the Hume-Rothery rule should be considered, such as the atomic radius, similar structure formation, and approximate electronegativity. A solubility parameter δ has already been identified to account for the enthalpy and atomic solubility of multicomponent materials [69]. Based on this parameter, high-entropy-alloyed multicomponent phases have been synthesized [69,80].

It is also worth noting that a high entropy doesn't guarantee a high ZT [66–68,80], as was observed in case of HEA $Sn_{0.25}Mn_{0.25}Ge_{0.25}Pb_{0.25}Te$ [69]. This is possibly because SnTe already crystallizes in a cubic (*Fm-3m*) structure, so the high entropy effect of improving the crystal symmetry by alloying for the PF enhancement is less effective. This was also the case for $(Cu/Ag)(In/Ga)Te_2$ [69].

Similarly, high-entropy alloying for a κ_L reduction is not very effective in compounds that already possess a low κ_L. For example, Cu_2Se possesses a κ_L close to the theoretical minimum κ_{min}, thus no significant decrease in κ_L can be achieved [69]. However, with an enhanced solubility limit due to adding suitable elements, severe lattice distortion was attained and a κ_L lower than κ_{min} was reported in Ref. [80]. Additionally, with an expanded phase space, multi-principal element alloying (MPEA) could be performed for the PF optimization. For example, an improved PF using band convergence caused by enhanced Mn solubility was obtained in $Sn_{0.555}Ge_{0.15}Pb_{0.075}Mn_{0.275}Te$ [81]. Another factor that can affect the TE performance is the number of alloying elements, because the increased mass

and strain fluctuations degrade the carrier mobility μ. Therefore, the number of elements should be optimized in a particular high-entropy-alloyed TE material so that any adverse effect on μ can be well compensated by the TE performance-enhanced entropy effects, such as a higher carrier concentration and band convergence.

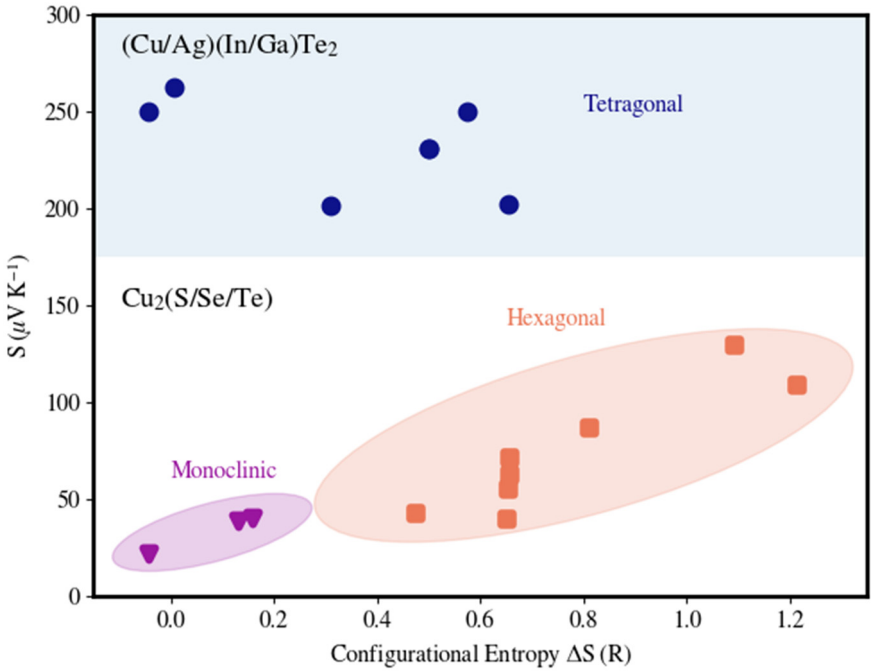

Figure 6. Changes in the monoclinic structure of Cu_2Se to hexagonal structures of $Cu_2S_{0.5}Te_{0.5}$, $Cu_2S_{0.5}Se_{0.5}$, and $Cu_2Se_{1/3}Te_{1/3}S_{1/3}$ using entropy alloying, leading to a significant increase in the thermopower with an increasing crystal lattice symmetry [recreated with permission of Ref. [69] copyright (2017), John Wiley and Sons].

Recent research demonstrated that entropy effects lead to impressive enhancements in the TE performance of several materials [75–89]. For example, a high peak ZT value of ~1.52 at 823 K and an average ZT value of ~1.0 from 323 to 823 K were obtained in $Ga_{0.025}(Sn_{0.25}Pb_{0.25}Mn_{0.25}Ge_{0.25})_{0.975}Te$. [81]. The increased configurational entropy, caused by the inclusion of various elements at the cationic (Sn^{2+}) site, led to an enhanced phonon scattering and a strongly suppressed κ_L. Similarly, a strong lattice distortion caused by the large difference in the atomic radii of Ag, Mn, Ge, and Sb in $AgMnGeSbTe_4$ HEA resulted in a κ_L as low as 0.54 W m^{-1} K^{-1} at 600 K [82]. The TE performance of $AgMnGeSbTe_4$ was further enhanced by the precipitation of Ag_8GeTe_6 (cocktail effect), which acted as extra scattering centers for the holes with low energy and phonons with medium wavelengths. This simultaneous optimization yielded a peak ZT of 1.27 at 773 K and an average ZT of 0.92 (400–773 K) in $AgMnGeSbTe_4$–(1 mol% Ag_8GeTe_6).

The configurational entropy-driven pseudo-binary diagram $AgBiSe_2$-PbSe was established recently [83]. The entropy effects simultaneously ensured the phase stability and maximized the ZT for the $(AgBiSe_2)_{1-x}(PbSe)_x$ solid solutions. Similarly, the high-entropy-alloyed $Pb_{0.89}Sb_{0.012}Sn_{0.1}Se_{0.5}Te_{0.25}S_{0.25}$ demonstrated an entropy-driven structural stabilization, ensuring the well-maintained electrical transport properties [84]. The large strains from the severely distorted lattice provided strong scattering for the heat-carrying phonons, contributing to an ultra-low κ_L and a consequent realization of a high ZT. For the high-entropy-alloyed metal chalcogenide $Ag_{0.25}Pb_{0.50}Bi_{0.25}S_{0.40}Se_{0.50}Te_{0.10}$, S_{mix} reached 2.00R, which exceeded the ideal value of S_{mix} = 1.79R for single-site alloying with six different elements [85,86]. However, research on $(CuAgInGa)_{0.5}Te_2$, $(CuAg)_{0.5}(AlGaIn)_{1/3}Te_2$ and $(CuAg)_{0.5}(ZnGeGaIn)_{0.25}Te_2$ indicated that simply pursuing the highest configuration entropy in TE materials cannot guarantee an improvement in the TE performance [90].

We conclude this section by emphasizing that high-entropy alloying disrupts the synthesis parameters that can significantly improve the TE properties. Although there have been many recent innovative advances and newly discovered materials, the synthesis parameters of the materials have remained unchanged for a few decades. The conventional selection rules of material composition were generally limited to small percentages of doping or alloying with one or two elements in the parent compounds. In this regard, high-entropy alloying provides a methodological breakthrough towards designing next-generation TE materials. The efficacy of the extended solubility limits provides a larger phase space for compositional alteration, and thus TE performance optimization. Improved TE materials may be engineered by adding new elements based on their formation energy and their ability to form similar structures.

3.2. Nanowires of Conventional TE Materials

Theoretically, nanowires (NWs) possess superior TE (electronic and thermal) properties compared to those of their bulk counterparts. Taking advantage of the intrinsic small size of NWs, TE devices can be manufactured using suitable processes both at single-NW and bulk scales. In this section, we will describe the various investigations on NWs composed of TE materials. The consideration of NWs for TE applications was largely inspired by the idea of quantum confinement proposed by Dresselhaus and Hicks [91,92], who investigated the PF and ZT of cylindrical Bi NWs through detailed calculations [93]. Later, NWs along with superlattices of quantum dots were synthesized [94–97] and calculations were conducted [98]. In 2003, a "suspended microbridge device"-based individual NW measurement technique was described [99]. Since then, TE studies of NWs have flourished and the ZT of individual NWs have been evaluated for several materials, such $Bi_{0.54}Te_{0.46}$ [100] and $CrSi_2$ [101]. However, these studies found that the nanowire ZT values did not improve with respect to their bulk counterparts. The probable reason behind this was a modest reduction in κ since a short l_{ph} is inherent to bulk chalcogenide and silicide materials. Hochbaum et al. [102] reported a significant improvement in the TE performance of individual rough Si NWs compared to bulk Si, reaching a ZT = 0.6 due to a 100-fold reduction in κ. Around the same time, Boukai et al. [103] also reported a $ZT \sim 1$ at 200 K for horizontally arrayed Si NWs. These Si NW arrays were produced using a different method from that of Ref. [102]. One major factor that became noticeable for ZT enhancement was the surface roughness and a further increase in ZT was expected by optimizing the doping and roughness conditions [104,105]. The ZT of the vertically oriented Si NW arrays at 300 K were found to be 0.11 [106] and 0.49 [107].

Improvements in the TE properties of these NWs were basically due to a reduction in κ_L resulting from phonon confinement. A higher ZT was achieved in NWs of relatively large diameters [108,109] through the combination of an inherently short l_{ph} and a high PF. This indicated that the size effect on the thermal transport was not very effective on materials that possess an inherently shorter l_{ph} [103,110–113]. No significant improvement was found in the individual NWs of materials that already present good bulk TE properties, such as Bi_2Te_3 [108–111], $CsSnI_3$ [108], Bi/Te [109], InSb [112], PbTe [113], $Bi_{0.5}Sb_{1.5}Te_3$ [114], $Si_{0.73}Ge_{0.27}$ [115], InSb [116], SnTe [117], and SnSe [118].

The other parameter which may hinder ZT in NWs is the low carrier mobility μ, because of the trap states and defects. Liang et al. [119] demonstrated an enhancement in the ZT of PbSe NWs by improving the carrier mobility with thermal annealing. Lee et al. reported a peak ZT of 0.46 at 450 K [114] for individual $Si_{0.73}Ge_{0.27}$ NWs and a ZT of 0.21 at room temperature. They found that the point defect scattering was more important than the NW diameter [120]. The collectively reported data for NWs demonstrated that, although the reasons may differ, size reduction is effective for achieving a higher ZT. It is true that a large enhancement in ZT has not yet been observed. Nevertheless, these concepts have led to several breakthroughs towards the understanding and enhancement of PFs in several TE materials.

New concepts, such as modulation doping in core shell heterostructures and inhomogeneous doping, have been implemented to boost the PF in NWs [25,121]. By using such concepts, new structures are being fabricated. For example, Davila et al. [122] produced vertically grown p-type and n-type silicon nanowires on two different substrates, which were added to fabricate a TE device (Figure 7a,b). They selectively grew highly dense and ordered arrays of Si NWs in a hexagonal shape (Figure 7c,d). Earlier, Yang et al. fabricated TE nanogenerators using Sb-doped ZnO individual nanobelts [123], whose ZT was found to reach 0.13. The power output of the TE generator constructed using a single nanobelt was ~1.94 nW under a temperature difference of 30 K around room temperature. Recently, an integrated macroscale TE chip of 1.0 × 2.0 cm^2 in size and composed of CdSSe nanowires was reported to be an excellent TEG [124]. A high Seebeck coefficient of -152.4 μV/K and an average output voltage of 10.8 mV were reported. More interestingly, the output voltage was greatly elevated to 45 mV upon illumination by white light due to the photogeneration of additional carriers. Additionally, in organic–inorganic interfaces composed of PEDOT:PSS shells with Te cores, a simultaneous κ reduction and PF enhancement was reported [125]. For the hybrid nanowire with the smallest diameter of 42 nm, the ZT values of 0.18 at 300 K and 0.54 at 400 K were achieved, where the latter was claimed to be the highest ZT value for the hybrid material. Recently, flexible thermoelectric materials have been synthesized, comprising Bi_2Te_3 [126] and Sb_2Te_3 [127] nanocrystals anchored/deposited on a single-walled carbon nanotube (SWCNT) network. For the Bi_2Te_3-coated SWCNT, an in-plane κ_L as low as 0.26 W/K-m was achieved, originating from a strong phonon scattering effect with a maximum ZT of 0.89 at 300 K [126]. In the Sb_2Te_3-coated SWCNT, a maximum PF of 59.5 μW/(m-K^2) was achieved, which was 4.7 times higher than the normal SWCNT film [127]. Similarly, the best performing flexible nanocomposite films of Bi_2Te_3 nanoplates and SWCNTs were also recently prepared [128]. These results illustrated the potential of these nanostructures and by using them as macroscale flexible thermoelectric chips, useful electric energy can be generated.

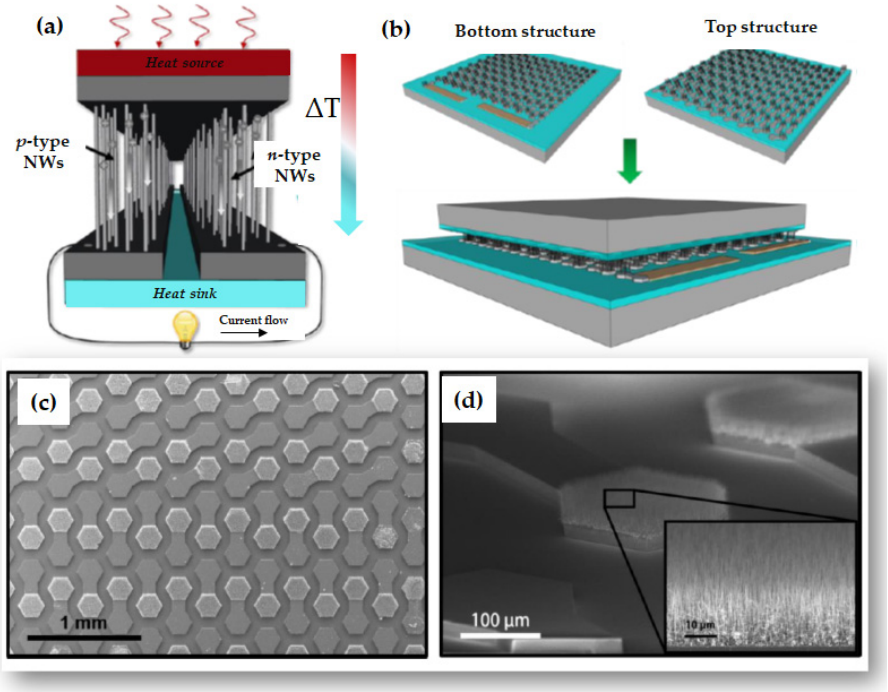

Figure 7. Schematic of (**a**) the fabrication of a TE device using (**b**) p-type and n-type silicon nanowires on two different substrates. (**c**) SEM image of the hexagonal TE elements (top and bottom structures). (**d**) Selectively grown, highly dense, and ordered arrays of Si NWs [reprinted with permission from ref. [122] under a Creative Commons Attribution license 3, Copyright (2015), IOPScience].

3.3. Topological Materials

Apart from the quantum size effects in conventional semiconductors, the recent TE research interest has been significantly focused on new types of quantum materials [e.g., Topological Insulators (TIs), weak TIs, Weyl, magnetic Weyl and Dirac semimetals] characterized by their nontrivial electronic topology. The recent experimental and theoretical studies [129–134] on semimetal WP_2 and $ZrTe_5$ nanostructures revealed a violation of the WF law, which could lead to the realization of a large ZT in topological materials. Future TE research will certainly need to be focused on such materials due to their significant and tunable quantum properties. Some excellent reviews are already available [135–138]. Here we will discuss the role of topological materials as TEs and the recent advances.

3.3.1. Topological Insulators

Topological insulators (TIs) are quantum materials that insulate the interior but feature a conducting surface or edge states that are topologically protected [139,140]. Such TIs offer a new route for designing high-performance TE devices [129–136,141–144]. In fact, some of the key concepts for designing a good TE material and a TI are quite similar. An optimum PF can be achieved using narrow band gap materials, whereas κ_L can be reduced using a combination of atoms with large and small atomic masses. Similarly, in Tis, the inverted band structure is combined with a narrow band gap. A TI material must have strong spin–orbit coupling, whose occurrence increases with the increasing atomic mass. Therefore, it is not a coincidence that TI compounds, such as tetradymites M_2X_3[138], where M is a group V element (usually Bi or Sb) and X is a group VI element (Te, Se or S), are also well-established TE materials, e.g., Bi_2Te_3, Sb_2Te_3, and Bi_2Se_3 [70,135,141,145–147]. All TIs with a bulk band gap and highly conductive and robust gapless surface states exhibit excellent TE properties. However, the reverse doesn't always follow, and some good TE materials are topologically trivial, such as PbTe [139,147]. Notwithstanding, the Sn-doped PbTe compounds ($Pb_{1-x}Sn_xTe$), which exhibit a good TE performance [148], were found to be topological crystalline insulators [149,150].

Although there is close relationship between the topological and TE properties, the positioning of ε_F differs in both materials. In TE materials, for the high-performance bulk transport properties, ε_F should be generally located at the edge of either the conduction or the valence bands. In TIs, it is important to shift ε_F to the Dirac point, so that the topological surface-state transport dominates and the contribution from the bulk state is suppressed [137]. However, Xu et al. [142] predicted an "anomalous Seebeck effect" in 2D TIs, even though ε_F is located near the conduction band when the relaxation time in the surface states (τ_s) is much higher than that of the bulk states (τ_b), $\tau_s \gg \tau_b$. They showed that the surface-state transport could outweigh the bulk-state transport and the ZT could be significantly larger than the unity by optimizing the geometric size. This indicated that the topological surface state-dominated transport properties could provide a new way for designing high performance TE devices.

Recently, theoretical calculations by Baldomir and Faílde [151] predicted that a new class of topological materials, with topological indices higher than one ($\overline{n} > 1$), could exceed the $ZT = 4$ level required for mainstream competitive TEs. For the edge states, the calculated [151] purely topological contribution to the figure of merit was as follows.

$$ZT_{TI} = \nu^2 \overline{n}^3 \frac{\pi_B^2}{3\zeta(3)} \tag{16}$$

where π_B is the Berry phase of the nontrivial material, ν counts the number of singularities, $\overline{n} = 1$ is the first Chern number (which takes into account the whole topology of the Brillouin zone for the TI), and $\zeta(3)$ is the Riemann zeta function of dimension three. This contribution to the ZT is zero in the case of topologically trivial materials. The expression was obtained considering only κ_e and under ideal conditions. Even though it is probable that, in practice,

the transport constraints may diminish the efficiency of such materials, this result provided a path towards the further improvement of ZT in TIs.

3.3.2. Weak Topological Insulators

A weak TI is a quantum state of matter that is equivalent to a stack of 2D TI layers with an even number of Dirac cones on the side surface [140,152–154]. The surface states of a weak TI are robust even under strong time-reversal (TR) invariant disorders [155], leading to a superior electronic transport. Weak TIs generally form a layered structure consisting of stacks of topologically nontrivial 2D quantum spin Hall (QSH) layers and topologically trivial/nontrivial normal insulator (NI) layers along a specific direction [140,152–155]. These NI layers play a critical role in hindering the phonon propagation, thereby leading to an ultra-low κ_L near room temperature [39,152]. Since weak TIs can be tuned to achieve an intrinsically ultra-low κ_L together with a decoupled electronic transport, high-performance TE materials can be designed using weak TIs; examples of which are $Bi_{14}Rh_3I_9$ [152], BiSe [39], and Bi_2TeI [152,156].

3.3.3. Dirac and Weyl Semimetals

Dirac [157,158] and Weyl [159–162] semimetals are relatively new classes of topological materials. These are gapless systems, since the conduction and valence bands touch linearly close to ε_F. Several such materials have been reported, including NbAs [159], NbP [160–163], Cd_3As_2 [164–168], TaAs [169,170], $Bi_{1-x}Sb_x$ [171,172], GdPtBi [173], and $MoTe_2$ [174]. In Dirac semimetals, the Dirac cone is degenerate, and both the time-reversal and inversion symmetries are preserved [157,158]. When one of these symmetries is broken, Weyl states emerge [175]. In momentum space, the band touching point splits into a pair of separated Weyl nodes with opposite chirality, leading to poor σ and S. This limitation can be overcome by changing the longitudinal Peltier configuration to the transverse Ettingshausen configuration, with the assistance of a magnetic field. Therefore, the ambipolar transport can be turned into a TE performance enhancer rather than a suppressor. The Ettingshausen configuration in semimetal Mg_2Pb has led to a much higher specific heat pumping power in the temperature range of 10–100 K [176]. The chiral symmetry can be violated at the quantum level when a magnetic field is applied in parallel either to an electric field (chiral anomaly) [158,173,176–178] or to a temperature gradient (gravitational anomaly, which is named since this anomaly originated in strong gravitational fields). These quantum anomalies induce an electrical/heat current which increases alongside an increasing magnetic field, leading to increased TE transport coefficients S, σ, and κ_e [177,179]. The existence of the chiral anomaly has been experimentally confirmed in semimetals using the anomalous Hall effect (AHE) and chiral magnetic effect (CME) [158,173,177,180].

A large transverse TE voltage (the Nernst effect) was found to appear in semimetals when a magnetic field was applied perpendicular to the temperature gradient [168,176,181–196]. The voltage was generated from electrons and holes and was deflected towards opposite transverse directions by the Lorentz force. The schematic of the thermopower generation from various phenomena are shown in Figure 8. The semimetals usually displayed a very high negative electrical magnetoresistance, thus providing another way to improve the PF under a magnetic field, potentially by two orders of magnitude. Liang et al. reported a Nernst thermopower of ~150 μV/K at 7.5 T in the Dirac semimetal $Pb_{0.77}Sn_{0.23}Se$ [181]. Later, a large and non-saturating thermopower in the Dirac and Weyl semimetals subjected to a quantized magnetic field was theoretically predicted by Skinner and Fu [197]. Wang et al. reported the TE properties of the single-crystalline Dirac semimetal Cd_3As_2 under magnetic fields and the ZT reached 1.1 at 350 K under a field of 7 T [187]. Similarly, a large Nernst signal was reported in Cd_3As_2 [168], leading to a higher Nernst figure of merit $ZT_N \approx 0.5$ at room temperature in a relatively small field of 2 T. Wang et al. reported a maximum ZT of 1.24 at 450 K in a magnetic field of 9 T in a study of Cd_3As_2 single crystals with various carrier concentrations [188]. Recently, a significantly large Nernst signal was reported in WTe_2 with a maximum 7000 μV/K at 11.3 K and 9 T [185]. The Ettingshausen

signal reached up to 5×10^{-5} $KA^{-1}m$ at 23.1 K and 9 T [185]. Earlier, Zhu et al. reported a value of approx. 3800 μV/K at 3.66 K and 17 T [189]. The theoretical calculations predicted very good *ZT* values of 0.82 and 0.50 along the *c* direction for p-type NbP and NbAs, respectively, at an optimal carrier concentration [190]. Earlier, for polycrystalline NbP [191], an unsaturated value of the Nernst thermopower of approx. 90 μV/K at 9 T and 136 K was attained, which was comparable to the conventional *S* of the TE materials. Remarkably, a large Nernst thermopower (617 μV/K at 14 T and 14 K) was achieved in polycrystalline $Mg_{3+\delta}Bi_2Mn_{0.025}$ [186]. The Nernst thermopowers at a given temperature and field of some promising semimetals, such as the Dirac semimetal Cd_3As_2 [168], $Mg_{2.33}Pb$ [176], type-II Weyl semimetal WTe_2 [185,189], $Pb_{1-x}Sn_xSe$ [181], NbP [190,191], (Zr, Hf)Te_5 [193–195], TbPtBi [196], $Mg_{3+\delta}Bi_2Mn_{0.025}$[186], and $YbMnSb_2$ [198] are listed in Table 1.

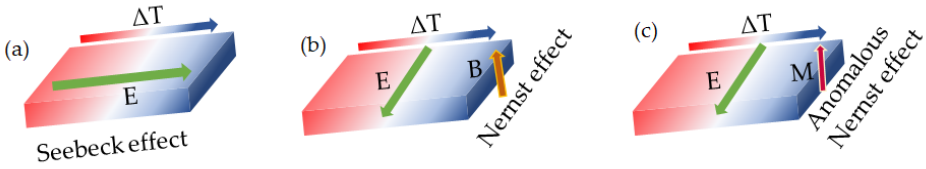

Figure 8. The schematic of the thermopower generation with (**a**) the Seebeck effect in normal materials, (**b**) the Nernst effect in topological semimetals, and (**c**) the anomalous Nernst effect in magnetic semimetals with a spontaneous magnetization M.

Table 1. Nernst thermopower reported for various semimetals at given temperatures and magnetic fields.

Semimetals	Crystal Structure/ Space Group	Temperature (K) and Magnetic Field (Tesla T)	Nernst Thermopower (μV/K)	References
Cd_3As_2	*Pnma*	250 K, 2 T	~126	[168]
$Mg_{2.33}Pb$	*Fm-3m*	30 K, 10T	~195	[176]
$Pb_{0.77}Sn_{0.23}Se$	*Pm-3m*	300 K, 7.5 T	150	[181]
WTe_2	*Pnm2*	11.3 K, 9 T	7000	[185]
		3.66 K, 17 T	~3800	[189]
$Mg_{3+\delta}Bi_2Mn_{0.025}$ (polycrystalline)	*Pm31*	14 K, 14 T	617	[186]
NbP	*I41md*	109 K, 9 T	800	[190]
NbP (polycrystalline)	*I41md*	136 K, 9 T	90	[191]
$ZrTe_5$	*Cmcm*	145 K, 6 T 110 K, 14 T	~440 ~1350	[193,194]
$HfTe_5$	*Cmcm*	100 K, 4 T	600	[195]
TbPtBi	*F-43m*	300 K, 13.5 T 150 K, 13.5 T	214 251	[196]
$YbMnSb_2$	*P4/nmm*	120 k, 14 T	40	[198]

Another intriguing property that could lead to a large *ZT* in semimetals is the violation of the WF law. The Lorenz ratio ($L = \kappa_e/\sigma T$) is the universal constant $L_0 = \kappa_e/\sigma = \pi^2k^2_B/3e^2$ for a given temperature where *e* is the charge of an electron. The figure of merit can then be rewritten as $ZT = S^2/(L + \sigma T\kappa_L)$. In semimetals, the electronic transport is due to electron–hole scattering, which leads to a more strongly relaxed thermal current than the electrical current. Suppressing the energy distribution of the conduction electrons with other carriers (holes) will decrease κ_e and, hence, decrease the ratio of κ_e/σ [134]. Thus, *L* decreases depending on the screening length of the Coulomb interaction. Takahashi et al. studied the transport coefficients of semimetals considering the impurity, electron–hole, and intra-band scatterings [133]. They showed that the TE coefficient of semimetals with

electron–hole scattering contained contributions beyond the relaxation time approximation in the transport theory, and S was largely enhanced.

The recently discovered topological ferromagnets (magnetic Weyl semimetals), such as Co_2MnGa [199,200] and $Co_3Sn_2S_2$ [201–203], have shown good TE properties under magnetic fields. These materials possess a large Berry curvature near ε_F [204]. The materials with large coercive fields (H_c) are candidates for observation of the Nernst effect at a zero field, since the remnant magnetization could work as an effective internal magnetic field. Therefore, similar to ferromagnets, these materials would also display a transverse voltage response under a thermal gradient, known as the anomalous Nernst effect (ANE) [205,206]. The schematic of the thermopower generation using the ANE is shown in Figure 8c. Single-crystalline $Co_3Sn_2S_2$ exhibited a maximum anomalous Nernst thermopower value of 3 μV/K at 80 K at the zero field, which was not sufficient for application, but significantly high considering its magnetic moment of only 0.89 μ_B/f.u. [202]. New, hard, magnetic topological materials with high Curie temperatures could suffice for this purpose. A room temperature anomalous Nernst signal of 2.1 μV/K (300 K, 1.5 T) was recently reported in Fe_3Sn_2 [207].

Another class of semimetals, known as topological nodal line semimetals (TNLSs), have been predicted as potential TE materials [208]. The combined effect of highly dispersive Dirac bands and regular bands led to a tenfold increase in the PF. The Dirac bands of $YbMnSb_2$ apparently provided a low resistivity along the direction in which they were highly dispersive. On the other hand, the density of the states provided by regular bands led to an S value exceeding 160 μV/K at 300 K. The asymmetry in the electronic band structures of semimetals, such as the disparities in the band effective mass and valley degeneracy between the conduction and valence bands, plus the accompanying electron-to-hole weighted mobility ratio (asymmetry in electron and hole mobilities), were responsible for their TE performance [209]. Such asymmetries were observed in various semiconductors [210] and are expected to occur in additional semimetals, providing a broad scope to establish high-performance quantum TE materials.

3.4. Nanowires of Topological Materials

It is expected that thin films and NWs of conventional TE materials will exhibit an improvement in their TE properties due to band structure manipulation. Xu et al. showed that the surface-state transport could outweigh the bulk state and the ZT could be significantly larger than the unity by optimizing the geometric size [142]. Their theoretical calculations also showed that a large ZT could be achieved in a TI NW when the Fermi surface was near the surface band gap [143]. A gap in the surface states could be opened when the thickness of a 3D TI NW is less than the penetration depth of the surface states [58,211,212]. The TE transport parameters can be enhanced by these surface-state narrow gaps that are analogous to the usual narrow gap semiconductors. These theoretical concepts can be verified by conducting transport experiments on TI thin films and nanowires. However, Bi_2Te_3, Bi_2Se_3, and Sb_2Te_3 with an increasing surface-to-volume ratio (*i.e.*, reduced dimensions) have shown poor TE properties due to the appearance of a more metallic character [213–215].

An anomalous sign of S was theoretically predicted [142] and then experimentally observed [216] in $(Bi_{1-x}Sb_x)_2Te_3$ thin films. Recent *ab initio* calculations claimed that ZT = 10 was achievable for single-layer TI $ZrTe_5$ nanoribbons [134]. The dramatic difference in the relaxation time between the backscattering-free in-gap topological edge states and the bulk states introduced several unusual TE phenomena, particularly an anomalous Seebeck effect [134,142,216] and a WF law violation [134,141]. Figure 9 shows the schematic diagrams of the (a) normal and (b) anomalous Seebeck effects. It can be seen from Equation (4) that the reduced $S\left(\frac{\varepsilon-\varepsilon_F}{k_BT}\right)$ is proportional to the dimensionless differential conductivity (DDC) $\left(-\frac{\partial f}{\partial \varepsilon}\right)\Sigma(\varepsilon)$, where the average is very close to ε_F for metals and lead to an S value that is smaller than the unity [134]. However, the anomalous Seebeck effect could be realized as a result of the long relaxation time of the topological states ($\tau_s \gg \tau_b$) below the

conduction band minimum (CBM). The much stronger scattering of the bulk-state carriers than that of the surface-state carriers effectively work as a carrier energy filtering, leading to a suppressed carrier transport around ε_F. The computational work on six quintuple-layer Bi_2Se_3 thin films [141] predicted a relaxation time in the order of hundreds of femtoseconds for the topological surface states, which was two orders higher in magnitude than that of the bulk states, which could then lead to a large anomalous Seebeck effect. On the other hand, the WF law violation was also predicted since the law connects the heat and charge transport of electrons in solids. Figure 9c shows a schematic for a normal metal DDC profile. In TI nanostructures, the DDC profile could be severely distorted (Figure 9d) due to the large difference in the carrier scattering intensity between the in-gap surface states and the bulk states, leading to small value of κ_e. This can lead to a significant violation of the WF law while maintaining a good TE performance through the in-gap surface states carriers [134,141].

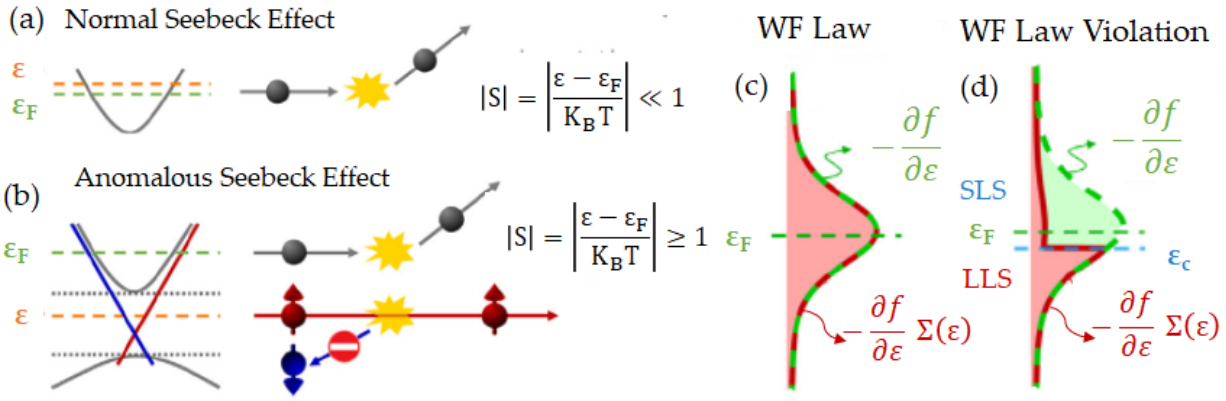

Figure 9. Schematics of (**a**) the reduced Seebeck coefficient in metals is less than unity because average of dimensionless differential conductivity (DDC) is very close to ε_F (normal Seebeck effect); (**b**) the calculated relaxation time for the topological surface states (LLS), is two orders higher in magnitude than that of the bulk states (SLS), leading to a large reduced Seebeck coefficient resulting anomalous Seebeck effect; (**c**) the normal metal DDC profile; and (**d**) the severely distorted DDC profile of TI nanostructures leads to large difference in the carrier scattering intensity between the LLS and the SLS, causing WF Law violation. [reprinted from with permission from Ref. [134], Copyright (2019), Elsevier].

The recent theoretical calculations proposed that thin films of TNLSs are promising TE materials [217]. When they are close to ε_F, the drumhead surface states of these materials result in a peculiar DOS structure, which can lead to a large and non-vanishing Seebeck coefficient. Unlike typical semiconductors, the surface states are robust against a disorder in the bulk, thus κ_L can, in principle, be reduced without a significant loss in the PF. A ZT greater than 13 for a five-layer film was reported, with the possibility of easily tuning the chemical potential by applying a gate voltage to the film, so the maximum ZT may be experimentally accessible. Furthermore, Ag_2S was suggested as a candidate for the realization of these theoretical predictions [217].

We can conclude from these sections on TI-based TE materials that, although the topological surface state-dominated TE transport properties are very challenging (for requiring an ideal system with well-modulated ε_F), the most recent experimental observations within new classes of TIs are encouraging [185,186,189]. The improvement of the TE performance requires a simultaneous enhancement of the PF and a reduction in κ_L. The calculations showed that by introducing disorder and defects in quintuple layers of Bi_2Te_3 [218] and controlling the geometric sizes in 2D TIs [144], the relative contributions of the electrons and phonons can be tuned for their optimum TE properties. Topological semimetals with a linear sharp-band dispersion could be excellent materials for achieving a high transverse Nernst thermopower [185].

4. Summary and Outlook

We presented a state-of-the-art quantum manipulation of thermoelectric (TE) materials for their performance enhancement. A simultaneous enhancement of the TE power factor and the suppression of the thermal conductivity can achieve competitive figures of merit ZT. In this regard, high-entropy-alloy (HEA)-based TE materials and nanowires (NWs) of TE materials have great potential to produce more efficient TE devices. The experimental band engineering methods and quantum confinement of the carriers/phonons have been instrumental for the NW TE performance. Considering the inherent challenges associated with NWs, an impressive TE performance has been achieved so far. Similarly, next-generation TE materials may be designed using HEAs, which can provide a methodological breakthrough for simultaneously employing band engineering methods alongside various phonon scattering mechanisms. Despite the challenging synthesis parameters of such materials, the extended solubility limit of elements provides a larger phase space for compositional alteration, and thus TE performance optimization. It can also be concluded that quantum materials, such as topological insulators (TIs) and their nanowires, can establish a solid foundation for revolutionizing TE research. Nontrivial topology materials with topological indices higher than the unity can surpass $ZT = 4$. The ab initio calculations showed that the Wiedemann–Franz law can be violated in topological semimetals and TI nano ribbons and also that $ZT = 10$ is achievable for single-layer nanoribbons of TIs. Topological semimetals with characteristics similar to that of WTe_2 (linear sharp-band dispersion) could be excellent materials for achieving a high transverse TE performance, and further theoretical and experimental studies should be performed. Topological magnetic semimetals, with asymmetry in the electronic band structures, provide a broad scope for prospecting novel, high-performance quantum TE materials as well.

The outlook for the next years is quite promising since a large and active community of researchers is currently involved worldwide. Breakthroughs in materials discovery/design, novel emergent phenomena, and performance benchmarks are continuously being achieved. For example, a giant ANE was found in the intermetallic compounds Fe_3Ga and Fe_3Al at room temperature [219]. The reported anomalous Nernst coefficients were as high as ~6 μV/K and ~4 μV/K, respectively, which are comparable to the topological magnetic semimetal Co_2MnGa [199]. The ANE originates from the Berry curvature of the conduction electrons near the ε_F that may be designed using nodal points and lines in momentum space. High-throughput computational research is now capable of helping to identify such materials, which optimizes, accelerates, and reduces the costs of these advances. Recently, Zhou et al. [220,221] found that an artificial hybridization of the Seebeck effect into the anomalous Hall effect enabled a transverse thermopower generation in a closed circuit comprising thermoelectric and magnetic materials. They demonstrated experimentally, using Co_2MnGa/Si hybrid materials, that the Seebeck-effect-driven transverse thermopower could reach several orders of magnitude higher than the ANE-driven thermopower. Novel approaches with magnetic materials are likely to become of great significance for heat-driven electrical energy generation and spin caloritronics. Searching for materials near room temperature remains of great interest for TE-driven cooling.

A great deal of synergetic theoretical and experimental research is still demanded to achieve both a fundamental understanding and a high-performance of TE devices. The energy materials research community looks forward to continued efforts to materialize current claims and to break new ground in TE research with this promising class of quantum materials.

Author Contributions: S.K.S.: writing—original draft, writing—review and editing, formal analysis; J.M.: review and editing, formal analysis; L.M.-F.: review and editing, formal analysis; M.A.A.: writing—original draft, writing—review and editing, formal analysis, visualization, project administration; resources. All authors have read and agreed to the published version of the manuscript.

Funding: We thank the São Paulo Research Foundation (FAPESP) for providing partial support to this work through the grants #2017/10581-1 and #2018/17384-0.

Data Availability Statement: Not applicable.

Acknowledgments: We thank the journals and publishers of Refs. [7,26,35,68,69,122,134] for giving their consent to republish and reproduce their figures.

Conflicts of Interest: The authors state no conflict of interest.

References

1. Bell, L.E. Cooling, Heating, Generating Power, and Recovering Waste Heat with Thermoelectric Systems. *Science* **2008**, *321*, 1457. [CrossRef] [PubMed]
2. Twaha, S.; Zhu, J.; Yan, Y.; Li, B. A comprehensive review of thermoelectric technology: Materials, applications, modelling and performance improvement. *Renew. Sustain. Energy Rev.* **2016**, *65*, 698. [CrossRef]
3. Snyder, G.; Toberer, E. Complex thermoelectric materials. *Nat. Mat.* **2008**, *7*, 105. [CrossRef]
4. Slack, G.A. *CRC Handbook of Thermoelectrics*; Rowe, D.M., Ed.; CRC Press: Boca Raton, FL, USA, 1995; p. 407.
5. Ioffe, A.F. *Semiconductor Thermoelements and Thermoelectric Cooling*; Infosearch: London, UK, 1957.
6. Kang, C.; Wang, H.; Bahk, J.; Kim, H.; Kim, W. *Hierarchical Nanostructures for Energy Devices*; Ko, S.H., Grigoropoulos, C.P., Eds.; The Royal Society of Chemistry: Cambridge, UK, 2014; pp. 107–141.
7. Han, C.; Sun, Q.; Li, Z.; Dou, S.X. Thermoelectric Enhancement of Different Kinds of Metal Chalcogenides. *Adv. Energy Mat.* **2016**, *6*, 1600498. [CrossRef]
8. Vining, C.B. An inconvenient truth about thermoelectrics. *Nat. Mater.* **2009**, *8*, 83. [CrossRef] [PubMed]
9. Shakouri, A. Recent Developments in Semiconductor Thermoelectric Physics and Materials. *Annu. Rev. Mater. Res.* **2011**, *41*, 399–431. [CrossRef]
10. LeBlanc, S.; Yee, S.K.; Scullin, M.L.; Dames, C.; Goodson, K.E. Material and manufacturing cost considerations for thermoelectrics. *Renew. Sustain. Energy Rev.* **2014**, *32*, 313–327. [CrossRef]
11. Shannon, K.Y.; LeBlanc, S.; Goodson, K.E.; Dames, C. $ per W metrics for thermoelectric power generation: Beyond ZT. *Energy Environ. Sci.* **2013**, *6*, 2561–2571.
12. Shakouri, A.; Zebarjadi, M. Nanoengineered Materials for Thermoelectric Energy Conversion. In *Thermal Nanosystems and Nanomaterials*; Volz, S., Ed.; Springer: Berlin/Heidelberg, Germany, 2009; pp. 225–299.
13. Xiao, Y.; Wang, D.; Zhang, Y.; Chen, C.; Zhang, S.; Wang, K.; Wang, G.; Pennycook, S.J.; Snyder, G.J.; Wu, H.; et al. Band Sharpening and Band Alignment Enable High Quality Factor to Enhance Thermoelectric Performance in n-Type PbS. *J. Am. Chem. Soc.* **2020**, *142*, 4051. [CrossRef]
14. Xiao, Y.; Wang, D.; Qin, B.; Wang, J.; Wang, G.; Zhao, L.D. Approaching Topological Insulating States Leads to High Thermoelectric Performance in n-Type PbTe. *J. Am. Chem. Soc.* **2018**, *140*, 13097. [CrossRef]
15. Hodges, J.M.; Hao, S.; Grovogui, J.A.; Zhang, X.; Bailey, T.P.; Li, X.; Gan, Z.; Hu, Y.Y.; Uher, C.; Dravid, V.P.; et al. Chemical Insights into PbSe−x%HgSe: High Power Factor and Improved Thermoelectric Performance by Alloying with Discordant Atoms. *J. Am. Chem. Soc.* **2018**, *140*, 18115. [CrossRef] [PubMed]
16. Luo, Z.Z.; Hao, S.; Cai, S.; Bailey, T.P.; Tan, G.; Luo, Y.; Spanopoulos, I.; Uher, C.; Wolverton, C.; Dravid, V.P.; et al. Enhancement of Thermoelectric Performance for n-Type PbS through Synergy of Gap State and Fermi Level Pinning. *J. Am. Chem. Soc.* **2019**, *141*, 6403. [CrossRef] [PubMed]
17. Luo, Z.Z.; Cai, S.; Hao, S.; Bailey, T.P.; Su, X.; Spanopoulos, I.; Hadar, I.; Tan, G.; Luo, Y.; Xu, J.; et al. High Figure of Merit in Gallium-Doped Nanostructured n-Type PbTe-xGeTe with Midgap States. *J. Am. Chem. Soc.* **2019**, *141*, 16169. [CrossRef] [PubMed]
18. Perumal, S.; Samanta, M.; Ghosh, T.; Shenoy, U.S.; Bohra, A.K.; Bhattacharya, S.; Singh, A.; Waghmare, U.V.; Biswas, K. Realization of High Thermoelectric Figure of Merit in GeTe by Complementary Co-doping of Bi and In. *Joule* **2019**, *3*, 2565. [CrossRef]
19. Hong, M.; Lyu, W.; Wang, Y.; Zou, J.; Chen, Z.-G. Establishing the Golden Range of Seebeck Coefficient for Maximizing Thermoelectric Performance. *J. Am. Chem. Soc.* **2020**, *142*, 2672. [CrossRef]
20. Cahill, D.G.; Watson, S.K.; Pohl, R. Lower limit to the thermal conductivity of disordered crystals. *Phys. Rev. B* **1992**, *46*, 6131. [CrossRef]
21. Rittner, E.S.; Neumark, G.F. Theoretical Bound on the Thermoelectric Figure of Merit of Two-Band Semiconductors. *J. Appl. Phys.* **1963**, *34*, 2071. [CrossRef]
22. Mahan, G.D.; Sofo, J.O. The Best Thermoelectric. *Proc. Natl. Acad. Sci. USA* **1996**, *93*, 7436. [CrossRef]
23. Tan, G.; Zhao, L.-D.; Kan, M.G. Rationally Designing High-Performance Bulk Thermoelectric. *Chem. Rev.* **2016**, *116*, 12123. [CrossRef]
24. Chen, G. *Nanoscale Energy Transport and Conversion: A Parallel Treatment of Electrons, Molecules, Phonons, and Photons*; Oxford University Press: Oxford, UK, 2005.
25. Chen, R.; Lee, J.; Lee, W.; Li, D. Thermoelectrics of Nanowires. *Chem. Rev.* **2019**, *119*, 9260. [CrossRef]
26. Zhao, W.; Liu, Z.; Sun, Z.; Zhang, Q.; Wei, P.; Mu, X.; Zhou, H.; Li, C.; Ma, S.; He, D.; et al. Superparamagnetic enhancement of thermoelectric performance. *Nature* **2017**, *549*, 247. [CrossRef] [PubMed]
27. Dyck, J.S.; Chen, W.; Yang, J.; Meisner, G.P.; Uher, C. Effect of Ni on the transport and magnetic properties of $Co_{1-x}Ni_xSb_3$. *Phys. Rev. B* **2002**, *65*, 115204. [CrossRef]

28. Li, X.Y.; Chen, L.D.; Fan, J.F.; Zhang, W.B. Thermoelectric properties of Te-doped $CoSb_3$ by spark plasma sintering. *J. Appl. Phys.* **2005**, *98*, 083702. [CrossRef]
29. Wang, S.; Yang, J.; Wu, L.; Wei, P.; Zhang, W.; Yang, J. On Intensifying Carrier Impurity Scattering to Enhance Thermoelectric Performance in Cr-Doped $Ce_yCo_4Sb_{12}$. *Adv. Funct. Mater.* **2015**, *25*, 6660. [CrossRef]
30. Suwardi, A.; Bash, D.; Ng, H.K.; Gomez, J.R.; Repaka, D.M.; Kumar, P.; Hippalgaonkar, K. Inertial effective mass as an effective descriptor for thermoelectrics via data-driven evaluation. *J. Mater. Chem. A* **2019**, *7*, 23762. [CrossRef]
31. Gibbs, Z.M.; Ricci, F.; Li, G.; Zhu, H.; Persson, K.; Ceder, G.; Hautier, G.; Jain, A.; Snyder, G.J. Effective mass and Fermi surface complexity factor from ab initio band structure calculations. *NPJ Comput. Mater.* **2017**, *3*, 8. [CrossRef]
32. Heremans, J.P.; Jovovic, V.; Toberer, E.S.; Saramat, A.; Kurosaki, K.; Charoenphakdee, A.; Yamanaka, S.; Snyder, G.J. Enhancement of Thermoelectric Efficiency in PbTe by Distortion of the Electronic Density of States. *Science* **2008**, *321*, 554. [CrossRef]
33. Zhang, Q.; Liao, B.; Lan, Y.; Lukas, K.; Liu, W.; Esfarjani, K.; Opeil, C.; Broido, D.; Chen, G.; Ren, Z. High Thermoelectric Performance by Resonant Dopant Indium in Nanostructured SnTe. *Proc. Natl. Acad. Sci. USA* **2013**, *110*, 13261. [CrossRef]
34. Heremans, J.P.; Wiendlocha, B.; Chamoire, A.M. Resonant Levels in Bulk Thermoelectric Semiconductors. *Energy Environ. Sci.* **2012**, *5*, 5510. [CrossRef]
35. Yang, J.; Xi, L.; Qiu, W.; Wu, L.; Shi, X.; Chen, L.; Yang, J.; Zhang, W.; Uher, C.; Singh, D.J. On the tuning of electrical and thermal transport in thermoelectrics: An integrated theory–experiment perspective. *NPJ Comput. Mater.* **2016**, *2*, 15015. [CrossRef]
36. Mao, J.; Liu, Z.; Ren, Z. Size effect in thermoelectric materials. *NPJ Quantum Mater.* **2016**, *1*, 16028. [CrossRef]
37. Born, M.; Von Karman, T. Vibrations in space gratings (molecular frequencies). *Z. Phys.* **1912**, *13*, 297.
38. Christensen, M.; Abrahamsen, A.B.; Christensen, N.B.; Juranyi, F.; Andersen, N.H.; Lefmann, K.; Andreasson, J.; Bahl, C.R.; Iversen, B.B. Avoided crossing of rattler modes in thermoelectric materials. *Nat. Mater.* **2008**, *7*, 811. [CrossRef]
39. Samanta, M.; Pal, K.; Pal, P.; Waghmare, U.V.; Biswas, K. Localized Vibrations of Bi Bilayer Leading to Ultralow Lattice Thermal Conductivity and High Thermoelectric Performance in Weak Topological Insulator n-Type BiSe. *J. Am. Chem. Soc.* **2018**, *140*, 5866. [CrossRef]
40. Morelli, D.T.; Jovovic, V.; Heremans, J.P. Intrinsically Minimal Thermal Conductivity in Cubic I-V-VI2 Semiconductors. *Phys. Rev. Lett.* **2008**, *101*, 035901. [CrossRef]
41. Liu, H.; Shi, X.; Xu, F.; Zhang, L.; Zhang, W.; Chen, L.; Li, Q.; Uher, C.; Day, T.; Snyder, G.J. Copper ion liquid-like thermoelectrics. *Nat. Mater.* **2012**, *11*, 422. [CrossRef]
42. Kim, S.I.; Lee, K.H.; Mun, H.A.; Kim, H.S.; Hwang, S.W.; Roh, J.W.; Yang, D.J.; Shin, W.H.; Li, X.S.; Lee, Y.H.; et al. Dense dislocation arrays embedded in grain boundaries for high-performance bulk thermoelectrics. *Science* **2015**, *348*, 109. [CrossRef] [PubMed]
43. Lin, S.; Li, W.; Li, S.; Zhang, X.; Chen, Z.; Xu, Y.; Chen, Y.; Pei, Y. High Thermoelectric Performance of Ag_9GaSe_6 Enabled by Low Cutoff Frequency of Acoustic Phonons. *Joule* **2017**, *1*, 816. [CrossRef]
44. Chandra, S.; Biswas, K. Realization of High Thermoelectric Figure of Merit in Solution Synthesized 2D SnSe Nanoplates via Ge Alloying. *J. Am. Chem. Soc.* **2019**, *141*, 6141. [CrossRef] [PubMed]
45. Vining, C.B. Silicon Germanium. In *CRC Handbook of Thermoelectrics*; Rowe, D.M., Ed.; CRC Press: London, UK, 1995.
46. Chen, Z.; Ge, B.; Li, W.; Lin, S.; Shen, J.; Chang, Y.; Hanus, R.; Snyder, G.J.; Pei, Y. Vacancy-induced dislocations within grains for high-performance PbSe thermoelectrics. *Nat. Commun.* **2017**, *81*, 3828. [CrossRef]
47. Chen, Z.; Jian, Z.; Li, W.; Chang, Y.; Ge, B.; Hanus, R.; Yang, J.; Chen, Y.; Huang, M.; Snyder, G.J.; et al. Lattice Dislocations Enhancing Thermoelectric PbTe in Addition to Band Convergence. *Adv. Mater.* **2017**, *29*, 1606768. [CrossRef] [PubMed]
48. Biswas, K.; He, J.; Blum, I.D.; Wu, C.-I.; Hogan, T.P.; Seidman, D.N.; Dravid, V.P.; Kanatzidis, M.G. High-Performance Bulk Thermoelectrics with All-Scale Hierarchical Architectures. *Nature* **2012**, *489*, 414. [CrossRef] [PubMed]
49. Wu, Y.; Chen, Z.; Nan, P.; Xiong, F.; Lin, S.; Zhang, X.; Chen, Y.; Chen, L.; Ge, B.; Pei, Y. Lattice Strain Advances Thermoelectrics. *Joule* **2019**, *3*, 1276. [CrossRef]
50. Appel, O.; Zilber, T.; Kalabukhov, S.; Beeri, O.; Gelbstein, Y. Morphological effects on the thermoelectric properties of $Ti_{0.3}Zr_{0.35}Hf_{0.35}Ni_{1+d}Sn$ alloys following phase separation. *J. Mater. Chem. C* **2015**, *31*, 1653.
51. Ziman, J.M. *Electrons and Phonons: The Theory of Transport Phenomena in Solids*; Oxford University Press: Oxford, UK, 1960.
52. Qiu, B.; Bao, H.; Ruan, X.; Zhang, G.; Wu, Y. Molecular dynamics simulations of lattice thermal conductivity and spectral phonon mean free path of Pbte: Bulk and nanostructures. *Comput. Mater. Sci.* **2012**, *53*, 278. [CrossRef]
53. Singh, S.K.; Avila, M.A. Minimization of thermal conductivity in nanostructures and geometric self-similar structures for thermoelectric applications. In *Rhythmic Advantages in Big Data and Machine Learning*; Springer Nature: Berlin/Heidelberg, Germany, 2020; pp. 71–93. [CrossRef]
54. Cowley, R.A. Anharmonic crystals. *Rep. Prog. Phys.* **1968**, *31*, 123. [CrossRef]
55. Banik, A.; Ghosh, T.; Arora, R.; Dutta, M.; Pandey, J.; Acharya, S.; Soni, A.; Waghmare, U.V.; Biswas, K. Engineering ferroelectric instability to achieve ultralow thermal conductivity and high thermoelectric performance in $Sn_{1-x}Ge_xTe$. *Energy Environ. Sci.* **2019**, *12*, 589. [CrossRef]
56. Li, C.; Ma, S.; Wei, P.; Zhu, W.; Nie, X.; Sang, X.; Sun, Z.; Zhang, Q.; Zhao, W. Magnetism-induced huge enhancement of the room-temperature thermoelectric and cooling performance of p-type BiSbTe alloys. *Energy Environ. Sci.* **2020**, *13*, 535. [CrossRef]
57. Ma, S.; Li, C.; Wei, P.; Zhu, W.; Nie, X.; Sang, X.; Zhao, W. High-pressure synthesis and excellent thermoelectric performance of Ni/BiTeSe magnetic nanocomposites. *J. Mater. Chem. A* **2020**, *8*, 4816–4826. [CrossRef]

58. Liu, C.-X.; Zhang, H.; Yan, B.; Qi, X.-L.; Frauenheim, T.; Dai, X.; Fang, Z.; Zhang, S.-C. Oscillatory crossover from two-dimensional to three-dimensional topological insulators. *Phys. Rev. B* **2010**, *81*, 041307. [CrossRef]
59. Zhao, W.; Wei, P.; Zhang, Q.; Peng, H.; Zhu, W.; Tang, D.; Yu, J.; Zhou, H.; Liu, Z.; Mu, X.; et al. Multi-localization transport behaviour in bulk thermoelectric materials. *Nat. Commun.* **2015**, *6*, 6197. [CrossRef] [PubMed]
60. You, L.; Liu, Y.; Li, X.; Nan, P.; Ge, B.; Jiang, Y.; Luo, P.; Pan, S.; Pei, Y.; Zhang, W.; et al. Boosting the Thermoelectric Performance of PbSe through Dynamic Doping and Hierarchical Phonon Scattering. *Energy Environ. Sci.* **2018**, *11*, 1848. [CrossRef]
61. Zhang, Y.; Zuo, T.T.; Tang, Z.; Gao, M.C.; Dahmen, K.A.; Liaw, P.K.; Lu, Z.P. Microstructures and properties of high-entropy alloys. *Prog. Mater. Sci.* **2014**, *61*, 11. [CrossRef]
62. Senkov, O.N.; Miller, J.D.; Miracle, D.B.; Woodward, C. Accelerated exploration of multi-principal element alloys with solid solution phases. *Nat. Commun.* **2015**, *6*, 6529. [CrossRef]
63. Yeh, J.W.; Chen, S.K.; Lin, S.J.; Gan, J.Y.; Chin, T.S.; Shun, T.T.; Tsau, C.-H.; Chang, S.Y. Nanostructured High-Entropy Alloys with Multiple Principal Elements: Novel Alloy Design Concepts and Outcomes. *Adv. Eng. Mater.* **2004**, *6*, 299. [CrossRef]
64. Zhang, F.; Zhang, C.; Chen, S.; Zhu, J.; Cao, W.; Kattner, U. An understanding of high entropy alloys from phase diagram calculations. *Calphad* **2014**, *45*, 1. [CrossRef]
65. Poon, S.J.; He, J. Multi-Principal-Element Approach to High-Performance Thermoelectric Materials. In *Materials Science and Materials Engineering*; Elsevier: Amsterdam, The Netherlands, 2019.
66. Miracle, D.B.; Senkov, O.N. A critical review of high entropy alloys and related concepts. *Acta Mater.* **2017**, *122*, 448. [CrossRef]
67. Shafeie, S.; Guo, S.; Hu, Q.; Fahlquist, H.; Erhart, P.; Palmqvist, A. High-entropy alloys as high-temperature thermoelectric materials. *J. Appl. Phys.* **2015**, *118*, 184905. [CrossRef]
68. George, E.P.; Deirek, R.; Ritchie, O.R. High Entropy Alloys. *Nat. Rev.* **2019**, *4*, 518. [CrossRef]
69. Liu, R.; Chen, H.; Zhao, K.; Qin, Y.; Jiang, B.; Zhang, T.; Sha, G.; Shi, X.; Uher, C.; Zhang, W.; et al. Entropy as a Gene-Like Performance Indicator Promoting Thermoelectric Materials. *Adv. Mater.* **2017**, *29*, 1702712. [CrossRef]
70. Kim, H.-S.; Heinz, N.A.; Gibbs, Z.M.; Tang, Y.; Kang, S.D.; Snyder, G.J. High thermoelectric performance in $(Bi_{0.25}Sb_{0.75})_2Te_3$ due to band convergence and improved by carrier concentration control. *Mater. Today* **2017**, *20*, 452. [CrossRef]
71. Tan, G.; Shi, F.; Hao, S.; Chi, H.; Bailey, T.P.; Zhao, L.D.; Uher, C.; Wolverton, C.; Dravid, V.P.; Kanatzidis, M.G. Valence Band Modification and High Thermoelectric Performance in SnTe Heavily Alloyed with MnTe. *J. Am. Chem. Soc.* **2015**, *137*, 11507. [CrossRef] [PubMed]
72. Zhu, T.; Liu, Y.; Fu, C.; Heremans, J.P.; Snyder, J.G.; Zhao, X. Compromise and Synergy in High-Efficiency Thermoelectric Materials. *Adv. Mater.* **2017**, *29*, 1605884. [CrossRef] [PubMed]
73. Zhang, J.; Liu, R.; Cheng, N.; Zhang, Y.; Yang, J.; Uher, C.; Shi, X.; Chen, L.; Zhang, W. High-Performance Pseudocubic Thermoelectric Materials from Non-cubic Chalcopyrite Compounds. *Adv. Mater.* **2014**, *26*, 3848. [CrossRef]
74. Liu, W.; Tan, X.; Yin, K.; Liu, H.; Tang, X.; Shi, J.; Zhang, Q.; Uher, C. Convergence of Conduction Bands as a Means of Enhancing Thermoelectric Performance of N-Type $Mg_2Si_{1-x}Sn_x$ Solid Solutions. *Phys. Rev. Lett.* **2012**, *108*, 166601. [CrossRef]
75. Liu, Y.; Xie, H.; Li, Z.; Zhang, Y.; Malliakas, C.D.; Al Malki, M.; Ribet, S.; Hao, S.; Pham, T.; Wang, Y.; et al. Dravid Unraveling the Role of Entropy in Thermoelectrics: Entropy-Stabilized Quintuple Rock Salt $PbGeSnCd_xTe_{3+x}$. *J. Am. Chem. Soc.* **2023**, *145*, 8677–8688.
76. Acharya, S.; Hwang, J.; Kim, K.; Kim, J.; Hwang, W.; Soon, A.; Kim, W. Quasi-random distribution of distorted nanostructures enhances thermoelectric performance of high-entropy chalcopyrite. *Nano Energy* **2023**, *112*, 108493. [CrossRef]
77. Roychowdhury, S.; Biswas, R.K.; Dutta, M.; Pati, S.K.; Biswas, K. Phonon Localization and Entropy-Driven Point Defects Lead to Ultralow Thermal Conductivity and Enhanced Thermoelectric Performance in $(SnTe)_{1-2x}(SnSe)_x(SnS)_x$. *ACS Energy Lett.* **2019**, *4*, 1658. [CrossRef]
78. Chen, R.; Jiang, Q.; Jiang, L.; Min, R.; Kang, H.; Chen, Z.; Guo, E.; Yang, X.; Wang, T. Entropy-driven multiscale defects enhance the thermoelectric properties of ZrCoSb-based half-Heusler alloys. *Chem. Eng. J.* **2023**, *455*, 140676. [CrossRef]
79. Zhang, Z.; Zhao, K.; Chen, H.; Ren, Q.; Yue, Z.; Wei, T.-R.; Qiu, P.; Chen, L.; Shi, X. Entropy engineering induced exceptional thermoelectric and mechanical performances in Cu2-yAgyTe1-2xSxSex. *Acta Mater.* **2022**, *224*, 117512. [CrossRef]
80. Hu, L.; Zhang, Y.; Wu, H.; Li, J.; Li, Y.; Mckenna, M.; He, J.; Liu, F.; Pennycook, S.J.; Zeng, X. Entropy Engineering of SnTe: Multi-Principal-Element Alloying Leading to Ultralow Lattice Thermal Conductivity and State-of-the-Art Thermoelectric Performance. *Adv. Energy Mater.* **2018**, *8*, 1802116. [CrossRef]
81. Wang, X.; Yao, H.; Zhang, Z.; Li, X.; Chen, C.; Yin, L.; Zhang, Q. Enhanced thermoelectric performance in high entropy alloys $Sn_{0.25}Pb_{0.25}Mn_{0.25}Ge_{0.25}Te$. *ACS Appl. Mater. Interfaces* **2021**, *13*, 18638–18647. [CrossRef] [PubMed]
82. Ma, Z.; Xu, T.; Li, W.; Cheng, Y.; Li, J.; Zhang, D.; Yang, J. High entropy semiconductor AgMnGeSbTe4 with desirable thermoelectric performance. *Adv. Funct. Mater.* **2021**, *31*, 2103197. [CrossRef]
83. Zhu, H.; Zhao, T.; Zhang, B.; An, Z.; Mao, S.; Wang, G.; Zhou, X. Entropy Engineered Cubic n-Type AgBiSe2 Alloy with High Thermoelectric Performance in Fully Extended Operating Temperature Range. *Adv. Energy Mater.* **2021**, *11*, 2003304. [CrossRef]
84. Jiang, B.; Yu, Y.; Cui, J.; Liu, X.; Xie, L.; Liao, J.; He, J. High-entropy-stabilized chalcogenides with high thermoelectric performance. *Science* **2021**, *371*, 830–834259. [CrossRef]
85. Yamashita, A.; Goto, Y.; Miura, A.; Moriyoshi, C.; Kuroiwa, Y.; Mizuguchi, Y. n-Type thermoelectric metal chalcogenide (Ag, Pb, Bi) (S, Se, Te) designed by multi-site-type high-entropy alloying. *Mater. Res. Lett.* **2021**, *9*, 366–372. [CrossRef]

86. Jiang, B.; Yu, Y.; Chen, H.; Cui, J.; Liu, X.; Xie, L.; He, J. Entropy engineering promotes thermoelectric performance in p-type chalcogenides. *Nat. Commun.* **2021**, *12*, 3234. [CrossRef] [PubMed]
87. Zhang, Q.; Guo, Z.; Wang, R.; Tan, X.; Song, K.; Sun, P.; Hu, H.; Cui, C.; Liu, G.-Q.; Jiang, J. High-Performance Thermoelectric Material and Module Driven by Medium-Entropy Engineering in SnTe. *Adv. Funct. Mater.* **2022**, *32*, 2205458. [CrossRef]
88. Zhang, P.; Lou, Z.; Gong, L.; Xu, J.; Chen, Q.; Reece, M.J.; Yan, H.; Dashevsky, Z.; Gao, F. High-entropy MTiO3 perovskite oxides with glass-like thermal conductivity for thermoelectric applications. *J. Alloys Compd.* **2023**, *937*, 168366. [CrossRef]
89. Shahabfar, S.; Xia, Y.; Morshedsolouk, M.H.; Mohammadi, M.; Naghavi, S.S. Synergistic effect of alloying on thermoelectric properties of two-dimensional PdPQ (Q = S, Se). *Phys. Chem. Chem. Phys.* **2023**, *25*, 9617–9625. [CrossRef]
90. Cai, J.; Yang, J.; Liu, G.; Wang, H.; Shi, F.; Tan, X.; Ge, Z.; Jiang, J. Ultralow thermal conductivity and improved ZT of CuInTe2 by high-entropy structure design. *Mater. Today Phys.* **2021**, *18*, 100394. [CrossRef]
91. Hicks, L.D.; Dresselhaus, M.S. Effect of quantum-well structures on the thermoelectric figure of merit. *Phys. Rev. B* **1993**, *47*, 12727. [CrossRef] [PubMed]
92. Hicks, L.D.; Dresselhaus, M.S. Thermoelectric figure of merit of a one-dimensional conductor. *Phys. Rev. B* **1993**, *47*, 16631. [CrossRef]
93. Lin, Y.M.; Sun, X.; Dresselhaus, M.S. Theoretical investigation of thermoelectric transport properties of cylindrical Bi nanowires. *Phys. Rev. B* **2000**, *62*, 4610. [CrossRef]
94. Dresselhaus, M.S.; Chen, G.; Tang, M.Y.; Yang, R.G.; Lee, H.; Wang, D.Z.; Ren, Z.F.; Fleurial, J.P.; Gogna, P. New Directions for Low—Dimensional Thermoelectric Materials. *Adv. Mater.* **2007**, *19*, 1043. [CrossRef]
95. Piraux, L.; George, J.M.; Despres, J.F.; Leroy, C.; Ferain, E.; Legras, R.; Ounadjela, K.; Fert, A. Giant magnetoresistance in magnetic multilayered nanowires. *Appl. Phys. Lett.* **1994**, *65*, 2484. [CrossRef]
96. Wu, Y.; Fan, R.; Yang, P. Block-by-Block Growth of Single-Crystalline Si/SiGe Superlattice Nanowires. *Nano Lett.* **2002**, *2*, 83. [CrossRef]
97. Gudiksen, M.S.; Lauhon, L.J.; Wang, J.; Smith, D.C.; Lieber, C.M. Growth of nanowire superlattice structures for nanoscale photonics and electronics. *Nature* **2002**, *415*, 617. [CrossRef]
98. Lin, Y.-M.; Dresselhaus, M.S. Thermoelectric properties of superlattice nanowires. *Phys. Rev. B* **2003**, *68*, 075304. [CrossRef]
99. Shi, L.; Li, D.; Yu, C.; Jang, W.; Kim, D.; Yao, Z.; Kim, P.; Majumdar, A. Measuring Thermal and Thermoelectric Properties of One-Dimensional Nanostructures Using a Microfabricated Device. *J. Heat Transf.* **2003**, *125*, 881. [CrossRef]
100. Zhou, J.; Jin, C.; Seol, J.H.; Li, X.; Shi, L. Thermoelectric Properties of Individual Electrodeposited Bismuth Telluride Nanowires. *Appl. Phys. Lett.* **2005**, *87*, 133109. [CrossRef]
101. Zhou, F.; Szczech, J.; Pettes, M.T.; Moore, A.L.; Jin, S.; Shi, L. Determination of Transport Properties in Chromium Disilicide Nanowires via Combined Thermoelectric and Structural Characterizations. *Nano Lett.* **2007**, *7*, 1649. [CrossRef]
102. Hochbaum, A.I.; Chen, R.; Diaz Delgado, R.; Liang, W.; Garnett, E.C.; Najarian, M.; Majumdar, A.; Yang, P. Enhanced thermoelectric performance of rough silicon nanowires. *Nature* **2008**, *451*, 163. [CrossRef] [PubMed]
103. Boukai, A.I.; Bunimovich, Y.; Tahir-Kheli, J.; Yu, J.-K.; Goddard, W.A., III; Heath, J.R. Silicon nanowires as efficient thermoelectric materials. *Nature* **2008**, *451*, 168. [CrossRef] [PubMed]
104. Martin, P.; Aksamija, Z.; Pop, E.; Ravaioli, U. Impact of Phonon-Surface Roughness Scattering on Thermal Conductivity of Thin Si Nanowires. *Phys. Rev. Lett.* **2009**, *102*, 125503. [CrossRef]
105. Lim, J.; Hippalgaonkar, K.; Andrews, S.C.; Majumdar, A.; Yang, P. Quantifying Surface Roughness Effects on Phonon Transport in Silicon Nanowires. *Nano Lett.* **2012**, *12*, 2475. [CrossRef] [PubMed]
106. Xu, B.; Khouri, W.; Fobelets, K. Two-Sided Silicon Nanowire Array/Bulk Thermoelectric Power Generator. *IEEE Electron Device Lett.* **2014**, *35*, 596.
107. Zhang, T.; Wu, S.; Xu, J.; Zheng, R.; Cheng, G. High thermoelectric figure-of-merits from large-area porous silicon nanowire arrays. *Nano Energy* **2015**, *13*, 433. [CrossRef]
108. Lee, W.; Li, H.; Wong, A.; Zhang, D.; Lai, M.; Yu, Y.; Kong, Q.; Lin, E.; Urban, J.J.; Grossman, J.C.; et al. Ultralow thermal conductivity in all-inorganic halide perovskites. *Proc. Natl. Acad. Sci. USA* **2017**, *114*, 8693. [CrossRef]
109. Kim, J.; Oh, M.W.; Kim, G.; Bahk, J.H.; Song, J.Y.; Jeon, S.G.; Chun, D.W.; Bae, J.-H.; Shim, W.; Lee, W. Strain-Engineered Allotrope-like Bismuth Nanowires for Enhanced Thermoelectric Performance. *Acta Mater.* **2018**, *144*, 145. [CrossRef]
110. Chen, C.L.; Chen, Y.Y.; Lin, S.J.; Ho, J.C.; Lee, P.C.; Chen, C.D.; Harutyunyan, S.R. Fabrication and Characterization of Electrodeposited Bismuth Telluride Films and Nanowires. *J. Phys. Chem. C* **2010**, *114*, 3385. [CrossRef]
111. Shin, H.S.; Jeon, S.G.; Yu, J.; Kim, Y.S.; Park, H.M.; Song, J.Y. Twin-driven thermoelectric figure-of-merit enhancement of Bi_2Te_3 nanowires. *Nanoscale* **2014**, *6*, 6158. [CrossRef] [PubMed]
112. Zhou, F.; Moore, A.L.; Pettes, M.T.; Lee, Y.; Seol, J.H.; Ye, Q.L.; Rabenberg, L.; Shi, L. Effect of growth base pressure on the thermoelectric properties of indium antimonide nanowires. *J. Phys. D Appl. Phys.* **2010**, *43*, 025406. [CrossRef]
113. Lee, S.H.; Shim, W.; Jang, S.Y.; Roh, J.W.; Kim, P.; Park, J.; Lee, W. Thermoelectric properties of individual single-crystalline PbTe nanowires grown by a vapor transport method. *Nanotechnology* **2011**, *22*, 295707. [CrossRef]
114. Lee, E.K.; Yin, L.; Lee, Y.; Lee, J.W.; Lee, S.J.; Lee, J.; Cha, S.N.; Whang, D.; Hwang, G.S.; Hippalgaonkar, K.; et al. Large Thermoelectric Figure-of-Merits from SiGe Nanowires by Simultaneously Measuring Electrical and Thermal Transport Properties. *Nano Lett.* **2012**, *12*, 2918. [CrossRef]

115. Li, L.; Xu, S.; Li, G. Enhancement of Thermoelectric Properties in Bi-Sb-Te Alloy Nanowires by Pulsed Electrodeposition. *Energy Technol.* **2015**, *3*, 825. [CrossRef]
116. Yazji, S.; Swinkels, M.Y.; De Luca, M.; A Hoffmann, E.; Ercolani, D.; Roddaro, S.; Abstreiter, G.; Sorba, L.; Bakkers, E.P.A.M.; Zardo, I. Assessing the thermoelectric properties of single InSb nanowires: The role of thermal contact resistance. *Semicond. Sci. Technol.* **2016**, *31*, 064001. [CrossRef]
117. Li, Z.; Xu, E.; Losovyj, Y.; Li, N.; Chen, A.; Swartzentruber, B.; Sinitsyn, N.; Yoo, J.; Jia, Q.; Zhang, S. Surface oxidation and thermoelectric properties of indium-doped tin telluride nanowires. *Nanoscale* **2017**, *9*, 13014. [CrossRef]
118. Hernandez, J.A.; Ruiz, A.; Fonseca, L.F.; Pettes, M.T.; Jose-Yacaman, M.; Benitez, A. Thermoelectric properties of SnSe nanowires with different diameters. *Sci. Rep.* **2018**, *8*, 11966. [CrossRef]
119. Liang, W.; Rabin, O.; Hochbaum, A.I.; Fardy, M.; Zhang, M.; Yang, P. Thermoelectric Properties of p-Type PbSe Nanowires. *Nano Res.* **2009**, *2*, 394. [CrossRef]
120. Kim, H.; Kim, I.; Choi, H.J.; Kim, W. Thermal conductivities of $Si_{1-x}Ge_x$ nanowires with different germanium concentrations and diameters. *Appl. Phys. Lett.* **2010**, *96*, 233106. [CrossRef]
121. Yang, H.; Bahk, J.-H.; Day, T.; Mohammed, A.M.S.; Snyder, G.J.; Shakouri, A.; Wu, Y. Enhanced Thermoelectric Properties in Bulk Nanowire Heterostructure-Based Nanocomposites through Minority Carrier Blocking. *Nano Lett.* **2015**, *15*, 1349. [CrossRef] [PubMed]
122. Davila, D.J.; Huber, R.; Hierold, C. Bottom-up Silicon Nanowire-Based Thermoelectric Microgenerators. *J. Phys. Conf. Ser.* **2015**, *660*, 012101. [CrossRef]
123. Yang, Y.; Pradel, K.C.; Jing, Q.; Wu, J.M.; Zhang, F.; Zhou, Y.; Zhang, Y.; Wang, Z.L. Thermoelectric Nanogenerators Based on Single Sb-Doped ZnO Micro/Nanobelts. *ACS Nano* **2016**, *6*, 6984. [CrossRef]
124. Ding, C.; Lu, T.; Wazir, N.; Ma, W.; Guo, S.; Xin, Y.; Li, A.; Liu, R.; Zou, B. New Type of Thermoelectric CdSSe Nanowire Chip. *ACS Appl. Mater. Interfaces* **2021**, *13*, 30959–30966. [CrossRef]
125. Lin, Y.; Gordon, M.P.; Menon, A.K.; Bruefach, A.; Haas, K.; Scott, M.C.; Prasher, R.S.; Urban, J.J. Decoupling electron and phonon transport in single-nanowire hybrid materials for high-performance thermoelectrics. *Sci. Adv.* **2021**, *7*, eabe6000.
126. Jin, Q.; Jiang, S.; Zhao, Y.; Wang, D.; Qiu, J.; Tang, D.-M.; Tan, J.; Sun, D.-M.; Hou, P.-X.; Chen, X.-Q.; et al. Flexible layer-structured Bi_2Te_3 thermoelectric on a carbon nanotube scaffold. *Nat. Mater* **2019**, *18*, 62–68. [CrossRef] [PubMed]
127. Eguchi, R.; Hoshino, K.; Takashiri, M. Sb_2Te_3 nanoparticle-containing single-walled carbon nanotube films coated with Sb_2Te_3 electrodeposited layers for thermoelectric applications. *Sci. Rep.* **2023**, *13*, 5783. [CrossRef]
128. Chiba, T.; Yabuki, H.; Takashiri, M. High thermoelectric performance of flexible nanocomposite films based on Bi_2Te_3 nanoplates and carbon nanotubes selected using ultracentrifugation. *Sci. Rep.* **2023**, *13*, 3010. [CrossRef]
129. Jaoui, A.; Fauqué, B.; Rischau, C.W.; Subedi, A.; Fu, C.; Gooth, J.; Kumar, N.; Süß, V.; Maslov, D.L.; Felser, C.; et al. Departure from the Wiedemann–Franz law in WP_2 driven by mismatch in *T*-square resistivity prefactors. *NPJ Quantum Mater.* **2018**, *3*, 64. [CrossRef]
130. Li, S.; Maslov, D.L. Lorentz ratio of a compensated metal. *Phys. Rev. B* **2018**, *98*, 245134. [CrossRef]
131. Zarenia, M.; Principi, A.; Vignale, G. Thermal transport in compensated semimetals: Effect of electron-electron scattering on Lorenz ratio. *Phys. Rev. B* **2020**, *102*, 214304. [CrossRef]
132. Lee, W.-R.; Michaeli, K.; Schwiete, G. Lorenz ratio of an impure compensated metal in the degenerate Fermi liquid regime. *Phys. Rev. B* **2021**, *103*, 115140. [CrossRef]
133. Takahashi, K.; Matsuura, H.; Maebashi, H.; Ogata, M. Thermoelectric properties in semimetals with inelastic electron-hole scattering. *Phys. Rev. B* **2023**, *107*, 115158. [CrossRef]
134. Wang, T.-H.; Jeng, H.-T. Topological insulator nanoribbons—A new paradigm for high thermoelectric performance. *Nano Energy* **2019**, *66*, 104092. [CrossRef]
135. Xu, N.; Xu, Y.; Zhu, J. Topological insulators for thermoelectrics. *NPJ Quantum Mater.* **2017**, *2*, 51. [CrossRef]
136. Gooth, J.; Schierning, G.; Felser, C.; Nielsch, K. Quantum materials for thermoelectricity. *MRS Bull.* **2018**, *43*, 18. [CrossRef]
137. Fu, C.; Sun, Y.; Felsar, C. Topological thermoelectrics. *APL Mater.* **2020**, *8*, 040913. [CrossRef]
138. Heremans, J.P.; Cava, R.J.; Samarth, N. Tetradymites as thermoelectrics and topological insulators. *Nat. Rev. Mater.* **2017**, *2*, 17049. [CrossRef]
139. Fu, L.; Kane, C.L. Topological insulators with inversion symmetry. *Phys. Rev. B* **2007**, *76*, 045302. [CrossRef]
140. Hasan, M.Z.; Kane, C.L. Colloquium: Topological Insulators. *Rev. Mod. Phys.* **2010**, *82*, 3045. [CrossRef]
141. Wang, T.-H.; Jeng, H.-T. Strongly Enhanced Thermoelectric Performance over a Wide Temperature Range in Topological Insulator Thin Films. *ACS Appl. Energy Mater.* **2018**, *1*, 5646. [CrossRef]
142. Xu, Y.; Gan, Z.X.; Zhang, S.-C. Enhanced Thermoelectric Performance and Anomalous Seebeck Effects in Topological Insulators. *Phys. Rev. Lett.* **2014**, *112*, 226801. [CrossRef] [PubMed]
143. Takahashi, R.; Murakami, S. Thermoelectric transport in topological insulators. *Semicond. Sci. Technol.* **2012**, *27*, 124005. [CrossRef]
144. Shi, H.; Parker, D.; Du, M.-H.; Singh, D.J. Connecting Thermoelectric Performance and Topological-Insulator Behavior: Bi_2Te_3 and Bi_2Te_2Se from First Principles. *Phys. Rev. Appl.* **2015**, *3*, 014004. [CrossRef]
145. Zhang, H.; Liu, C.X.; Qi, X.L.; Dai, X.; Fang, Z.; Zhang, S.C. Topological insulators in Bi_2Se_3, Bi_2Te_3 and Sb_2Te_3 with a single Dirac cone on the surface. *Nat. Phys.* **2009**, *5*, 438. [CrossRef]

146. Hsieh, D.; Xia, Y.; Qian, D.; Wray, L.; Meier, F.; Dil, J.H.; Osterwalder, J.; Patthey, L.; Fedorov, A.V.; Lin, H.; et al. Observation of Time-Reversal-Protected Single-Dirac-Cone Topological-Insulator States in Bi_2Te_3 and Sb_2Te_3. *Phys. Rev. Lett.* **2009**, *103*, 146401. [CrossRef]
147. Müchler, L.; Yan, B.; Casper, F. Topological Insulators. In *Thermoelectric Nanomaterials: Materials Design and Applications*; Koumoto, K., Mori, T., Eds.; Springer-Verlag: Berlin/Heidelberg, Germany, 2013.
148. Ben-Ayoun, D.; Sadia, Y.; Gelbstein, Y. High temperature thermoelectric properties evolution of $Pb_{1-x}Sn_xTe$ based alloys. *J. Alloys Compd.* **2017**, *722*, 33. [CrossRef]
149. Tanaka, Y.; Ren, Z.; Sato, T.; Nakayama, K.; Souma, S.; Takahashi, T.; Segawa, K.; Ando, Y. Experimental realization of a topological crystalline insulator in SnTe. *Nat. Phys.* **2012**, *8*, 800. [CrossRef]
150. Xu, S.-Y.; Liu, C.; Alidoust, N.; Neupane, M.; Qian, D.; Belopolski, I.; Denlinger, J.D.; Wang, Y.J.; Lin, H.; Wray, L.A.; et al. Observation of a topological crystalline insulator phase and topological phase transition in $Pb_{1-x}Sn_xTe$. *Nat. Commun.* **2012**, *3*, 1192. [CrossRef]
151. Baldomir, D.; Faílde, D. On Behind the Physics of the Thermoelectricity of Topological Insulators. *Sci. Rep.* **2019**, *9*, 6324. [CrossRef] [PubMed]
152. Wei, P.; Yang, J.; Guo, L.; Wang, S.; Wu, L.; Xu, X.; Zhao, W.; Zhang, Q.; Zhang, W.; Dresselhaus, M.S.; et al. Minimum Thermal Conductivity in Weak Topological Insulators with Bismuth-Based Stack Structure. *Adv. Funct. Mater.* **2018**, *26*, 5360. [CrossRef]
153. Yan, B.; Müchler, L.; Felser, C. Prediction of Weak Topological Insulators in Layered Semiconductors. *Phys. Rev. Lett.* **2012**, *109*, 116406. [CrossRef]
154. Rasche, B.; Isaeva, A.; Ruck, M.; Borisenko, S.; Zabolotnyy, V.; Büchner, B.; Koepernik, K.; Ortix, C.; Richter, M.; Van Den Brink, J. Stacked topological insulator built from bismuth-based graphene sheet analogues. *Nat. Mater.* **2013**, *12*, 422. [CrossRef] [PubMed]
155. Mong RS, K.; Bardarson, J.H.; Moore, J.E. Quantum Transport and Two-Parameter Scaling at the Surface of a Weak Topological Insulator. *Phys. Rev. Lett.* **2012**, *108*, 076804. [CrossRef]
156. Tu, K.; Wei, P.; Zhou, H.; Mu, X.; Zhu, W.; Nie, X.; Zhao, W. A Thermoelectric Performance Study of Layered Bi2TeI Weak Topological Insulator Materials. *Energies* **2018**, *11*, 891. [CrossRef]
157. Moll, P.J.; Nair, N.L.; Helm, T.; Potter, A.C.; Kimchi, I.; Vishwanath, A.; Analytis, J.G. Transport evidence for Fermi-arc-mediated chirality transfer in the Dirac semimetal Cd_3As_2. *Nature* **2016**, *535*, 266. [CrossRef]
158. Xiong, J.; Kushwaha, S.K.; Liang, T.; Krizan, J.W.; Hirschberger, M.; Wang, W.; Cava, R.J.; Ong, N.P. Evidence for the chiral anomaly in the Dirac semimetal Na_3Bi. *Science* **2015**, *350*, 413. [CrossRef]
159. Xu, S.Y.; Alidoust, N.; Belopolski, I.; Yuan, Z.; Bian, G.; Chang, T.R.; Zheng, H.; Strocov, V.N.; Sanchez, D.S.; Chang, G.; et al. Discovery of a Weyl fermion state with Fermi arcs in niobium arsenide. *Nat. Phys.* **2015**, *11*, 748. [CrossRef]
160. Shekhar, C.; Nayak, A.K.; Sun, Y.; Schmidt, M.; Nicklas, M.; Leermakers, I.; Zeitler, U.; Skourski, Y.; Wosnitza, J.; Liu, Z.; et al. Extremely large magnetoresistance and ultrahigh mobility in the topological Weyl semimetal candidate NbP. *Nat. Phys.* **2015**, *11*, 645. [CrossRef]
161. Sergelius, P.; Gooth, J.; Bäßler, S.; Zierold, R.; Wiegand, C.; Niemann, A.; Reith, H.; Shekhar, C.; Felser, C.; Yan, B.; et al. Berry phase and band structure analysis of the Weyl semimetal NbP. *Sci. Rep.* **2016**, *6*, 33859. [CrossRef] [PubMed]
162. Niemann, A.C.; Gooth, J.; Wu, S.-C.; Bäßler, S.; Sergelius, P.; Hühne, R.; Rellinghaus, B.; Shekhar, C.; Süß, V.; Schmidt, M.; et al. Chiral magnetoresistance in the Weyl semimetal NbP. *Sci. Rep.* **2017**, *7*, 43394. [CrossRef] [PubMed]
163. Gooth, J.; Niemann, A.C.; Meng, T.; Grushin, A.G.; Landsteiner, K.; Gotsmann, B.; Menges, F.; Schmidt, M.; Shekhar, C.; Süß, V.; et al. Experimental signatures of the mixed axial–gravitational anomaly in the Weyl semimetal NbP. *Nature* **2017**, *547*, 324. [CrossRef] [PubMed]
164. Hosseini, T.; Yavarishad, N.; Alward, J.; Kouklin, N.; Gajdardziska-Josifovska, M. Large Thermopower, Crystalline Cd_3As_2 by Low-Temperature Vapor Deposition for Room Temperature Heat Waste Recovery. *Adv. Electron. Mater.* **2016**, *21*, 500319.
165. Jia, Z.; Li, C.; Li, X.; Shi, J.; Liao, Z.; Yu, D.; Wu, X. Thermoelectric signature of the chiral anomaly in Cd_3As_2. *Nat. Commun.* **2016**, *7*, 13013. [CrossRef]
166. Zhang, C.; Zhou, T.; Liang, S.; Cao, J.; Yuan, X.; Liu, Y.; Shen, Y.; Wang, Q.; Zhao, J.; Xiu, F. Unexpected low thermal conductivity and large power factor in Dirac semimetal Cd_3As_2. *Chin. Phys. B* **2015**, *25*, 017202. [CrossRef]
167. Xiang, J.; Hu, S.; Lv, M.; Zhang, J.; Zhao, H.; Chen, G.; Li, W.; Chen, Z.; Sun, P. Enhanced thermoelectric properties of the Dirac semimetal Cd_3As_2. *Inorg. Chem. Front.* **2016**, *31*, 637.
168. Xiang, J.; Hu, S.; Lyu, M.; Zhu, W.; Ma, C.; Chen, Z.; Steglich, F.; Chen, G.; Sun, P. Large transverse thermoelectric figure of merit in a topological Dirac semimetal. *Sci. China Phys. Mech. Astron.* **2020**, *63*, 237011. [CrossRef]
169. Xiang, J.; Hu, S.; Lv, M.; Zhang, J.; Zhao, H.; Chen, G.; Li, W.; Chen, Z.; Sun, P. Anisotropic thermal and electrical transport of Weyl semimetal TaAs. *J. Phys. Condens. Matter.* **2017**, *29*, 485501. [CrossRef]
170. Peng, B.; Zhang, H.; Shao, H.; Lu, H.; Zhang, D.W.; Zhu, H. High thermoelectric performance of Weyl semimetal TaAs. *Nano Energy* **2016**, *30*, 225. [CrossRef]
171. Shin, D.; Lee, Y.; Sasaki, M.; Jeong, Y.H.; Weickert, F.; Betts, J.B.; Kim, H.-J.; Kim, K.-S.; Kim, J. Violation of Ohm's law in a Weyl metal. *Nat. Mater.* **2017**, *16*, 1096. [CrossRef] [PubMed]
172. Kim, H.-J.; Kim, K.-S.; Wang, J.-F.; Sasaki, M.; Satoh, N.; Ohnishi, A.; Kitaura, M.; Yang, M.; Li, L. Dirac versus Weyl Fermions in Topological Insulators: Adler-Bell-Jackiw Anomaly in Transport Phenomena. *Phys. Rev. Lett.* **2013**, *111*, 246603. [CrossRef] [PubMed]

173. Hirschberger, M.; Kushwaha, S.; Wang, Z.; Gibson, Q.; Liang, S.; Belvin, C.A.; Bernevig, B.A.; Cava, R.J.; Ong, N.P. The chiral anomaly and thermopower of Weyl fermions in the half-Heusler GdPtBi. *Nat. Mater.* **2016**, *15*, 1161. [CrossRef] [PubMed]
174. Jiang, J.; Liu, Z.; Sun, Y.; Yang, H.; Rajamathi, C.; Qi, Y.; Yang, L.; Chen, C.; Peng, H.; Hwang, C.-C.; et al. Signature of type-II Weyl semimetal phase in $MoTe_2$. *Nat. Commun.* **2017**, *8*, 13973. [CrossRef]
175. Kim, P.; Ryoo, J.H.; Park, C.-H. Breakdown of the Chiral Anomaly in Weyl Semimetals in a Strong Magnetic Field. *Phys. Rev. Lett.* **2017**, *119*, 266401. [CrossRef]
176. Chen, Z.; Zhang, X.; Ren, J.; Zeng, Z.; Chen, Y.; He, J.; Chen, L.; Pei, Y. Leveraging bipolar effect to enhance transverse thermoelectricity in semimetal Mg_2Pb for cryogenic heat pumping. *Nat. Commun.* **2021**, *12*, 3837. [CrossRef]
177. Lundgren, R.; Laurell, P.; Fiete, G.A. Thermoelectric properties of Weyl and Dirac semimetals. *Phys. Rev. B* **2014**, *90*, 165115. [CrossRef]
178. Huang, X.; Zhao, L.; Long, Y.; Wang, P.; Chen, D.; Yang, Z.; Liang, H.; Xue, M.; Weng, H.; Fang, Z.; et al. Observation of the Chiral-Anomaly-Induced Negative Magnetoresistance in 3D Weyl Semimetal TaAs. *Phys. Rev. X* **2015**, *5*, 031023. [CrossRef]
179. Lucas, A.; Davison, R.A.; Sachdev, S. Hydrodynamic theory of thermoelectric transport and negative magnetoresistance in Weyl semimetals. *Proc. Natl. Acad. Sci. USA* **2016**, *113*, 9463. [CrossRef]
180. Burkov, A.A. Chiral anomaly and transport in Weyl metals. *J. Phys. Condens. Matter* **2015**, *27*, 113201. [CrossRef]
181. Liang, T.; Gibson, Q.; Xiong, J.; Hirschberger, M.; Koduvayur, S.P.; Cava, R.J.; Ong, N.P. Evidence for massive bulk Dirac fermions in $Pb_{1-x}Sn_xSe$ from Nernst and thermopower experiments. *Nat. Commun.* **2013**, *4*, 2696. [CrossRef] [PubMed]
182. Sharma, G.; Goswami, P.; Tewari, S. Nernst and magnetothermal conductivity in a lattice model of Weyl fermions. *Phys. Rev. B* **2016**, *93*, 035116. [CrossRef]
183. Liang, T.; Lin, J.; Gibson, Q.; Gao, T.; Hirschberger, M.; Liu, M.; Cava, J.; Ong, N.P. Anomalous Nernst Effect in the Dirac Semimetal Cd_3As_2. *Phys. Rev. Lett.* **2017**, *118*, 136601. [CrossRef] [PubMed]
184. Ferreiros, Y.; Zyuzin, A.A.; Bardarson, J.H. Anomalous Nernst and thermal Hall effects in tilted Weyl semimetals. *Phys. Rev. B* **2017**, *96*, 115202. [CrossRef]
185. Pan, Y.; He, B.; Helm, T.; Chen, D.; Schnelle, W.; Felser, C. Ultrahigh transverse thermoelectric power factor in flexible Weyl semimetal WTe_2. *Nat. Commun.* **2022**, *13*, 3909. [CrossRef]
186. Feng, T.; Wang, P.; Han, Z.; Zhou, L.; Wang, Z.; Zhang, W.; Liu, Q.; Liu, W. Large Transverse and Longitudinal Magneto-Thermoelectric Effect in Polycrystalline Nodal-Line Semimetal Mg_3Bi_2. *Energy Environ. Sci.* **2023**, *16*, 1560–1568. [CrossRef]
187. Wang, H.; Luo, X.; Chen, W.; Wang, N.; Lei, B.; Meng, F.; Shang, C.; Ma, L.; Wu, T.; Dai, X.; et al. Magnetic-field enhanced high-thermoelectric performance in topological Dirac semimetal Cd_3As_2 crystal. *Sci. Bull.* **2018**, *63*, 411. [CrossRef]
188. Wang, H.; Luo, X.; Peng, K.; Sun, Z.; Shi, M.; Ma, D.; Wang, N.; Wu, T.; Ying, J.; Wang, Z.; et al. Magnetic Field-Enhanced Thermoelectric Performance in Dirac Semimetal Cd_3As_2 Crystals with Different Carrier Concentrations. *Adv. Funct. Mater.* **2019**, *29*, 1902437. [CrossRef]
189. Zhu, Z.; Lin, X.; Liu, J.; Fauque, B.; Tao, Q.; Yang, C.; Shi, Y.; Behnia, K. Quantum Oscillations, Thermoelectric Coefficients, and the Fermi Surface of Semimetallic WTe_2. *Phys. Rev. Lett.* **2015**, *114*, 176601. [CrossRef]
190. Zhou, Y.; Zhao, Y.Q.; Zeng, Z.Y.; Chen, X.R.; Geng, H.Y. Anisotropic thermoelectric properties of Weyl semimetal NbX (X = P and As): A potential thermoelectric material. *Phys. Chem. Chem. Phys.* **2019**, *21*, 15167–15176. [CrossRef]
191. Fu, C.; Guin, S.N.; Watzman, S.J.; Li, G.; Liu, E.; Kumar, N.; Su, V.; Schnelle, W.; Auffermann, G.; Shekhar, C.; et al. Large Nernst power factor over a broad temperature range in polycrystalline Weyl semimetal NbP. *Energy Environ. Sci.* **2018**, *11*, 2813. [CrossRef]
192. Watzman, S.J.; McCormick, T.M.; Shekhar, C.; Wu, S.-C.; Sun, Y.; Prakash, A.; Felser, C.; Trivedi, N.; Heremans, J.P. Dirac dispersion generates unusually large Nernst effect in Weyl semimetals. *Phys. Rev. B* **2018**, *97*, 161404. [CrossRef]
193. Zhang, J.L.; Wang, C.M.; Guo, C.Y.; Zhu, X.D.; Zhang, Y.; Yang, J.Y.; Wang, Y.Q.; Qu, Z.; Pi, L.; Lu, H.-Z.; et al. Anomalous Thermoelectric Effects of $ZrTe_5$ in and beyond the Quantum Limit. *Phys. Rev. Lett.* **2019**, *123*, 196602. [CrossRef] [PubMed]
194. Zhang, W.; Wang, P.; Skinner, B.; Bi, R.; Kozii, V.; Cho, C.-W.; Zhong, R.; Schneeloch, J.; Yu, D.; Gu, G.; et al. Observation of a thermoelectric Hall plateau in the extreme quantum limit. *Nat. Commun.* **2020**, *11*, 1046. [CrossRef]
195. Hu, J. Large magneto thermopower and anomalous Nernst effect in $HfTe_5$. *Phys. Rev. B* **2019**, *100*, 115201. [CrossRef]
196. Wang, H.; Zhou, Z.; Ying, J.; Xiang, Z.; Wang, R.; Wang, A.; Chai, Y.; He, M.; Lu, X.; Han, G.; et al. Large Magneto-Transverse and Longitudinal Thermoelectric Effects in the Magnetic Weyl Semimetal TbPtBi. *Adv. Mater.* **2023**, *35*, 2206941. [CrossRef] [PubMed]
197. Skinnier, B.; Fu, L. Large, nonsaturating thermopower in a quantizing magnetic field. *Sci. Adv.* **2018**, *4*, eaat2621. [CrossRef]
198. Xu, S.; Jiang, C.; Li, S.X.; Mi, J.-J.; Li, Z.; Xia, T.-L.; Tao, Q.; Xu, Z.-A. Large Nernst effect and possible temperature-induced Lifshitz transition in topological semi metal YbMnSb2. *Phys. Rev. B* **2023**, *107*, 245138. [CrossRef]
199. Belopolski, I.; Manna, K.; Sanchez, D.S.; Chang, G.; Ernst, B.; Yin, J.; Zhang, S.S.; Cochran, T.; Shumiya, N.; Zheng, H.; et al. Discovery of topological Weyl fermion lines and drumhead surface states in a room temperature magnet. *Science* **2019**, *365*, 1278. [CrossRef]
200. Sakai, A.; Mizuta, Y.P.; Nugroho, A.A.; Sihombing, R.; Koretsune, T.; Suzuki, M.-T.; Takemori, N.; Ishii, R.; Nishio-Hamane, D.; Arita, R.; et al. Giant anomalous Nernst effect and quantum-critical scaling in a ferromagnetic semimetal. *Nat. Phys.* **2018**, *14*, 1119–1124. [CrossRef]
201. Morali, N.; Batabyal, R.; Nag, P.K.; Liu, E.; Xu, Q.; Sun, Y.; Yan, B.; Felser, C.; Avraham, N.; Beidenkopf, H. Fermi-arc diversity on surface terminations of the magnetic Weyl semimetal $Co_3Sn_2S_2$. *Science* **2019**, *365*, 1286–1291. [CrossRef]

202. Guin, S.N.; Vir, P.; Zhang, Y.; Kumar, N.; Watzman, S.J.; Fu, C.; Liu, E.; Manna, K.; Schnelle, W.; Gooth, J.; et al. Zero-Field Nernst Effect in a Ferromagnetic Kagome-Lattice Weyl-Semimetal $Co_3Sn_2S_2$. *Adv. Mater.* **2019**, *31*, 1806622. [CrossRef] [PubMed]
203. Geishendorf, K. Signatures of the Magnetic Entropy in the Thermopower Signals in Nanoribbons of the Magnetic Weyl Semimetal $Co_3Sn_2S_2$. *Nano Lett.* **2020**, *20*, 300–305. [CrossRef] [PubMed]
204. Das, K.; Agarwal, A. Berry curvature induced thermopower in type-I and type-II Weyl semimetals. *Phys. Rev. B* **2019**, *100*, 0854069. [CrossRef]
205. Boona, S.R.; Myers, R.C.; Heremans, J.P. Spin caloritronics. *Energy Environ. Sci.* **2014**, *7*, 885. [CrossRef]
206. Miyasato, T.; Abe, N.; Fujii, T.; Asamitsu, A.; Onoda, S.; Onose, Y.; Nagaosa, N.; Tokura, Y. Crossover Behavior of the Anomalous Hall Effect and Anomalous Nernst Effect in Itinerant Ferromagnets. *Phys. Rev. Lett.* **2007**, *99*, 086602. [CrossRef]
207. Zhang, H.; Xu, C.Q.; Ke, X. Topological Nernst effect, anomalous Nernst effect, and anomalous thermal Hall effect in the Dirac semimetal Fe_3Sn_2. *Phys. Rev. B* **2021**, *103*, L201101. [CrossRef]
208. Pan, Y.; Fan, F.R.; Hong, X.; He, B.; Le, C.; Schnelle, W.; Felser, C. Thermoelectric properties of novel semimetals: A case study of $YbMnSb_2$. *Adv. Mater.* **2021**, *33*, 2003168. [CrossRef]
209. Mao, J.; Chen, G.; Ren, Z. Thermoelectric cooling materials. *Nat. Mater.* **2021**, *20*, 454–461. [CrossRef]
210. Sze, S.M.; Ng, K.K. *Physics of Semiconductor Devices*; Wiley: New York, NY, USA, 2006.
211. Linder, J.; Yokoyama, T.; Sudbø, A. Anomalous finite size effects on surface states in the topological insulator Bi_2Se_3. *Phys. Rev. B* **2009**, *80*, 205401. [CrossRef]
212. Lu, H.-Z.; Shan, W.-Y.; Yao, W.; Niu, Q.; Shen, S.-Q. Massive Dirac fermions and spin physics in an ultrathin film of topological insulator. *Phys. Rev. B* **2010**, *81*, 115407. [CrossRef]
213. Gooth, J.; Gluschke, J.G.; Zierold, R.; Leijnse, M.; Linke, H.; Nielsch, K. Thermoelectric performance of classical topological insulator nanowires. *Semicond. Sci. Technol.* **2015**, *30*, 015015. [CrossRef]
214. Hamdou, B.; Gooth, J.; Dorn, A.; Pippel, E.; Nielsch, K. Surface state dominated transport in topological insulator Bi_2Te_3 nanowires. *Appl. Phys. Lett.* **2013**, *103*, 193107. [CrossRef]
215. Hinsche, N.F.; Zastrow, S.; Gooth, J.; Pudewill, L.; Zierold, R.; Rittweger, F.; Rauch, T.; Henk, J.; Nielsch, K.; Mertig, I. Impact of the Topological Surface State on the Thermoelectric Transport in Sb_2Te_3 Thin Films. *ACS Nano* **2015**, *9*, 4406. [CrossRef]
216. Zhang, J.; Feng, X.; Xu, Y.; Guo, M.; Zhang, Z.; Ou, Y.; Feng, Y.; Li, K.; Zhang, H.; Wang, L.; et al. Disentangling the magnetoelectric and thermoelectric transport in topological insulator thin films. *Phys. Rev. B* **2015**, *91*, 075431. [CrossRef]
217. Hosoi, M.; Tateishi, I.; Matsuura, H.; Ogata, M. Thin films of topological nodal line semimetals as a candidate for efficient thermoelectric converters. *Phys. Rev. B* **2022**, *105*, 085406. [CrossRef]
218. Liang, J.; Cheng, L.; Zhang, J.; Liu, H.; Zhang, Z. Maximizing the thermoelectric performance of topological insulator Bi2Te3 films in the few-quintuple layer regime. *Nanoscale* **2016**, *8*, 8855–8862. [CrossRef]
219. Sakai, A.; Minami, S.; Koretsune, T.; Chen, T.; Higo, T.; Wang, Y.; Nomoto, T.; Hirayama, M.; Miwa, S.; Nishio-Hamane, D.; et al. Iron-based binary ferromagnets for transverse thermoelectric conversion. *Nature* **2020**, *581*, 53–57. [CrossRef]
220. Zhou, W.; Yamamoto, K.; Miura, A.; Iguchi, R.; Miura, Y.; Uchida, K.-I.; Sakuraba, Y. Seebeck-driven transverse thermoelectric generation. *Nat. Mater.* **2021**, *20*, 463–467. [CrossRef]
221. Zhou, W.; Miura, A.; Hirai, T.; Sakuraba, Y.; Uchida, K.I. Seebeck-driven transverse thermoelectric generation in magnetic hybrid bulk materials. *Appl. Phys. Lett.* **2023**, *122*, 062402. [CrossRef]